Supplementary Materials for

A human-driven decline in global burned area

N. Andela,* D. C. Morton, L. Giglio, Y. Chen, G. R. van der Werf, P. S. Kasibhatla, R. S. DeFries, G. J. Collatz, S. Hantson, S. Kloster, D. Bachelet, M. Forrest, G. Lasslop, F. Li, S. Mangeon, J. R. Melton, C. Yue, J. T. Randerson

*Corresponding author. Email: niels.andela@nasa.gov

Published 30 June 2017, *Science* **356**, 1356 (2017)
DOI: 10.1126/science.aal4108

This PDF file includes:

Other Supplementary Materials for this manuscript include the following:
(available at www.sciencemag.org/content/356/6345/1356/suppl/DC1)

FireMIP data

Materials and Methods

Observing fire dynamics from space

Fire is a fundamental component of the Earth system. It is estimated that global annual burned area exceeds the size of the European Union (464 Mha yr^{-1}, *26*). Most burned area occurs in grasslands and savannas, where fire plays a major role in nutrient and carbon cycling (*2*, *41*). Despite burning less frequently, forest fires and fires associated with deforestation and peat burning contribute about half of global emissions because these fires have higher levels of fuel consumption (*27*, *42*).

There are two widely used but fundamentally different ways to observe fires from space. First, burned area can be mapped using time series of satellite imagery. The extent of burned area provides a direct estimate of the extent of fire impacts, and burned areas in many ecosystems can be detected for many weeks after the fire has occurred, avoiding issues related to fire detection during periods of cloud cover or smoke obscuration (*43*). A second approach is to identify actively burning fires in satellite imagery by isolating hot pixels from surrounding cooler pixels. Active fire observations in the form of counts or observations of fire radiative power (FRP) are related to the amount of biomass burned, and can thus be used to generate estimates of fuel consumption (*44*). Depending on the instrument, active fire measurements are also able to observe relatively small fires that often fall below the detection limit of burned area products derived from moderate resolution surface reflectance imagery (*29*).

We used two global satellite-derived burned area products in our analysis. First, the Global Fire Emissions Database Version 4 estimate of burned area including small fires (GFED4s) combines burned area and active fire detections to characterize global fire activity from 1997 – 2016 (*26*, *27*, *43*). The GFED4s burned area time series uses the 500-m MCD64A1 collection 5.1 burned area product as its primary data layer, and incorporates the contribution of small fires to burned area at 0.25° monthly resolution (*27*; ~37% of total burned area) using information from active fire detections mapped outside of 500-m burned areas. Active fire detections from the Tropical Rainfall Measuring Mission (TRMM) Visible and Infrared Scanner (VIRS) and the Along-Track Scanning Radiometer (ATSR) were used to extend the time series back to 1997, before the start of the Moderate resolution Imaging Spectroradiometer (MODIS) data record in 2000 (*27*, *42*). As described below in more detail, we used the GFED4s data to estimate fire trends for the 1998 – 2015 fire years, where at each 0.25° grid cell we identified the fire year as starting 5 months before and 6 months after the climatological mean month of maximum burning.

The second burned area dataset we used in our analysis was the MODIS global burned area product (MCD64A1 collection 5.1), an estimate of daily changes in surface reflectance from fire activity at the MODIS 500-m spatial resolution (*29*, *43*). The MCD64A1 dataset provides a consistent global record of larger fires (≥21 ha) since August 2000, and the 500-m daily resolution data can be used to study the size distribution of individual fires and explore the global extent of fire-prone ecosystems. In this study, we used MCD64A1 data from August 2002 through June 2016, a period when the combination of data from NASA's MODIS instruments onboard the Terra and Aqua satellites offered greater cloud-free data coverage. We used the MCD64A1 burned area data to estimate fire trends for the 2003 – 2015 fire years.

Precipitation-induced variation and trends

Seasonal and inter-annual variability in rainfall has a first-order impact on burned area, and controlling for precipitation variability is critical for assessing regional trends in fire activity that are driven by processes other than climate variability. Statistical models have been used previously to study the influence of precipitation on vegetation dynamics (*45–49*), fire activity (*50*), burned area (*11*, *15*), and fire forecasts (*51*). Higher levels of precipitation prior to the onset of the fire season may increase fire activity in arid regions because greater moisture availability enhances herbaceous biomass production and thus fuel buildup and continuity, whereas higher levels of precipitation during the fire season may suppress fires because of increases in fuel moisture (*50*). Both effects can occur within the same region, with their relative importance depending on the timing and magnitude of precipitation anomalies. Although these two contrasting effects may affect burned area in a single grid cell, they rarely exhibit significant effects at the same time (*15*). In general, precipitation has a negative correlation with burned area on short lead times in humid savannas and tropical forests and a positive correlation over longer time scales in more xeric savannas and grasslands. Therefore, we followed *Andela and van der Werf* (*15*) and used a single precipitation – burned area response that was optimized separately for each grid cell to prevent over fitting.

In this study, we investigated precipitation-induced variation and trends in burned area data using a linear model. Below, we summarize the modeling approach using MCD64A1 burned area data and results (Fig. S1); the same model with different optimized parameters was used to investigate precipitation-induced variation and trends in GFED4s burned area as well as time series of the number and size of fires derived from MCD64A1 burned area data.

Precipitation data were used as the only explanatory variable. Data from TRMM 0.25° monthly product 3B43 version 7 (1998 – 2015, 50°N – 50°S, *52*) was the primary source of precipitation data, and Global Precipitation Climatology Project (GPCP) 2.5° monthly product version 2.3 data (1979 – 2015, global coverage, *53*, *54*) were used outside the TRMM domain (e.g., at high latitudes and globally during 1996 – 1997).

We defined the burning season for each 0.25° grid cell as centered on the all-year mean (climatology) month of maximum burned area (i.e., from 5 months before until 6 months after the month of maximum burned area). Then, we explored the relationship between antecedent precipitation and burned area during the burning season based on the lead time before the month of maximum burned area. For each grid cell (x, y) and year (t) we calculated the antecedent precipitation (AP), defined as the mean monthly precipitation (*P*) during 1 to 24 months prior to the month of maximum burned area (m):

$$AP_{x,y,t} = \frac{\sum_{i=m-T_{x,y}}^{i=m-1} P_{x,y,i}}{T_{x,y}}. \quad (1)$$

Where *AP* is the antecedent precipitation and *T* is the antecedent precipitation accumulation period (1 – 24 months). This analysis yielded 24 annual time series of *AP* along with a single annual time series of burned area (BA) data. Subsequently, the burned area and AP time series were detrended using linear regression such that each time series can be given by:

$$BA = BA_{IAV} + BA_{TREND}, \text{ and} \quad (2)$$
$$AP = AP_{IAV} + AP_{TREND}. \quad (3)$$

BA_{TREND} and AP_{TREND} include both intercept and slope terms such that BA_{IAV} and AP_{IAV} can be considered trend-corrected anomalies.

While burned area trends may be caused by a range of drivers, inter-annual variability (IAV) in burned area is strongly related to precipitation. Therefore, we selected the BA and AP IAV time series to optimize our model and explore the relationship between antecedent precipitation and burned area. For each grid cell (x,y), we created a no-intercept linear regression model for each of the 24 AP_{IAV} time series:

$$BA_{IAV\,x,y,t} = b0_{x,y} \times AP_{IAV\,x,y,t} + \varepsilon_{x,y,t}, \quad (4)$$

where $b0_{x,y}$ is the optimally-fitted parameter to minimize the sum of the least square errors ($\varepsilon_{x,y,t}$). In addition, we calculated the correlation of the regression models using each of the 24 antecedent precipitation (AP_{IAV}) time series. The model that resulted in the largest absolute correlation (positive or negative) was selected to determine the precipitation-induced variation and trends in burned area (Fig. S1). We defined the antecedent precipitation index (API) as the accumulated precipitation anomaly time series (including both trend and IAV) using the lead time (*T*) for which the model based on AP_{IAV} (eq. 4) showed the largest absolute correlation (positive or negative) with BA_{IAV}, such that the precipitation-induced variation and trends in burned area can be written as:

$$BA_{precipitation} = b0_{x,y} \times API_{x,y,t}, \quad (5)$$

and the precipitation adjusted (PA) burned area time series as:

$$BA_{PA} = BA_{IAV} + BA_{trend} - BA_{precipitation} = BA - BA_{precipitation}. \quad (6)$$

We estimated precipitation-induced variability and trends in burned area at 0.25° resolution for all grid cells. However, fire size cannot be estimated for grid cells and years without burned area. Therefore, we modeled precipitation-induced variability and trends in the number of fires and fire size at 0.25° resolution for frequently-burning grid cells or at coarser resolution for regions with less frequent fire activity. To assure robust model performance, and account for missing data in the fire size time series in regions with infrequent burning, we selected a minimum burned area threshold (5 km^2 yr^{-1}). For individual 0.25° grid cells that did not meet this threshold, we analyzed the response of fire to precipitation using clusters of adjacent grid cells. The maximum cluster size was set to 2.5° × 2.5° (i.e., one hundred 0.25° grid cells). To determine the cluster size, we first identified all 0.25° grid cells within the larger 2.5° regions with burned area greater than or equal to 5 km^2 yr^{-1}. These grid cells were classified as

single grid cell clusters. In the next step, all remaining grid cells were grouped at 0.5° resolution and the 0.5° clusters with burned area ≥5 km^2 yr^{-1} were separated, similar to the previous step. The clustering analysis was repeated for 1.25° regions, and finally for the entire 2.5° region. Remaining grid cells within the 2.5° × 2.5° region that together did not meet the threshold (<5 km^2 yr^{-1}) or entire 2.5° × 2.5° regions with burned area below 5 km^2 yr^{-1} were excluded from our analysis, excluding about 6% of global annual burned area, mostly in the arid subtropics and boreal forests.

Separating individual fires using daily 500-m burned area data

High-resolution daily burned area data from MCD64A1 allowed us to quantify important statistical characteristics of fires, including fire number and the distribution of individual fire sizes (Fig. S2). This information provided new insight regarding the drivers of observed trends in burned area. Here, we extended the work of *Archibald et al.* (*55*) to develop an algorithm to distinguish individual fires and characterize their attributes.

We identified individual fires using the MCD64A1 500-m daily burned area product from August 2002 through June 2016 (*29*). This data range corresponds to fire years 2003 – 2015, as the time series analysis was based on the fire season burned area for each pixel, centered on the month of maximum burning. During this period, the MCD64A1 product combines data from MODIS instruments onboard the Aqua and Terra satellites; multiple overpasses per day provide a more robust estimate of the day of burn (i.e., due to obscuration by clouds or smoke) and avoid gaps in data coverage from the Terra MODIS sensor (most notably December 16 – 24 2003 and February 18 – 28 2016).

We developed an algorithm to isolate individual fires based on the day of burn information from the MCD64A1 product and regional thresholds for fire spread rates. Our approach differs from *Archibald et al.* (*55*) because we allowed a large burn scar to be comprised of multiple smaller fires, a common situation in frequently burning savannas. Our approach identified individual fires using local minima in the estimated day of burn from MCD64A1 and maximum fire spread rates—the time (in days) needed for a fire to spread from one 500-m grid cell into the next (*56*, here referred to as "fire persistence" with units of days).

A spatially-varying fire persistence threshold was used to separate individual fires based on fire frequency (Fig. S2a). If the fire persistence threshold is too long, fires burning in two adjacent pixels may be erroneously joined, for example in agricultural regions where two neighboring fields are burnt within the same week. On the other hand, fire spread rates may be slow in regions with high fuel loads (including forests), especially if fires persist in a smoldering state during periods of unfavorable weather conditions for burning. A short fire persistence threshold may therefore erroneously split one fire into two or more individual fires. In addition, cloud cover and orbital coverage contribute to uncertainty in the burn date assigned to individual pixels in the burned area product (*43*). A spatially-varying fire persistence threshold was selected to account for differences in fire spread rates and the influence of fire persistence on estimates of the number and size of individual fires. Frequently burning areas are generally characterized by fine fuels that allow fires to spread rapidly, with limited smoldering after the passage of the fire front. In addition, in regions with frequent fire activity, the statistical chance of another fire occurring in the vicinity is higher. Therefore, we used a 2-day fire persistence period for 500-m grid cells with fire return periods <5 years (based on 2001 – 2015 data), and gradually increased the fire persistence threshold for grid cells with longer fire return periods: 3 days for 5 – 7.5 years, 4 days for 7.5 – 15 years and 5 days for >15 years. Mean fire persistence at 0.25° resolution is shown in Fig. S2a, while Fig. S2b and S2c show the resulting estimates of the mean annual number of fires and mean fire size per 0.25° grid cell, respectively. Global distributions of the number and size of fires from this approach were highly correlated with previous work (on a logarithmic scale, we found $r^2 = 0.57$ for fire number and $r^2 = 0.56$ for fire size) using an alternate MODIS burned area product, MCD45 (*57*).

Global trends in burned area, number of fires, and fire size

We analyzed trends in burned area separately for the GFED4s (1998 – 2015) and MCD64A1 (2003 – 2015) time series (Table 1, S1 and Fig. S3). In all instances except for the comparison with the data from the Fire Model Intercomparison Project (FireMIP), trends were calculated using per burning season annual time series of burned area (defined as 5 months before until 6 months after the month of maximum burned area). To construct the 18-year GFED4s time series, we therefore used burned area data from August 1997 through June 2016, while the MCD64A1 analysis used data from August 2002 through June 2016. In the northern hemisphere tropics, the burning season is typically divided over two calendar years, with peak burned area around December or January. Using per burning season time series of burned area, rather than per calendar year data, thus allows for more robust estimates of burned area trends and was required for our precipitation-driven burned area model. For comparisons with global fire model outputs from FireMIP, we used calendar year burned area to estimate trends to match the annual format of burned area estimates from the models (Table S2, Fig. 3, S8 and S10).

Our model of precipitation-induced variability and trends captured the influence of climate on regional burned area dynamics, and information on the number and size of individual fires provided information on the drivers of observed changes in burned area. We calculated trends using simple linear regression, and we estimated the 95% confidence interval of the regression slopes and their significance using t-tests with two-tailed p-values. For the trend analysis, we assumed that uncertainties in burned area were constant over time. In case of the GFED4s time series, uncertainties were likely larger during the pre-MODIS years, but the absolute uncertainties remain difficult to characterize.

We analyzed trend statistics for multiple time intervals to directly compare burned area information from different sources and to evaluate the robustness of observed burned area trends after excluding pre-MODIS burned area estimates. The magnitudes of burned area trends varied depending on the time interval of the analysis but the global decrease in burned area was robust across all analyses. We used normalized time series to estimate the relative contributions from changes in the number and size of fires to overall burned area trends (Fig. 2 and S7; data were normalized to 2003 values, with values in 2003 set equal to 1). We used MODIS vegetation continuous field data (MOD44B collection 5, *58*) from the year 2000 to assess burned area trends as a function of tree cover. We calculated both mean burned area and burned area trends per fractional tree cover bin, based on 5% increments of tree cover, including all vegetated grid cells (Fig. 1, excluding grid cells with greater than 50% of non-vegetated areas or water). Finally, we compared observed trends in burned area to observed trends in the sum of Terra and Aqua MODIS active fire counts (2003 – 2015, MOD14 and MYD14 collection 6 datasets) as an additional source of data on changes in global biomass burning (Fig. S4a).

Comparison to global fire models

We compared trends in satellite-based estimates of burned area with output from global fire models within state-of-the-art ecosystem models (Table 1, Table S2, Fig. 3, S8 – S10 and S14). We included all FireMIP models (*34*, *59*) for which data was available on 1 October 2016, and compared modeled burned area to GFED4s burned area over the period of overlapping data availability (for 1997 – 2013 calendar years). FireMIP currently includes 9 global fire models: CLM fire module (*60*, *61*), LPJ-GUESS-SIMFIRE-BLAZE (*34*, *62*), LPJ-GUESS-GlobFIRM (*63*), LPJ-GUES-SPITFIRE (*64*), ORCHIDEE-SPITFIRE (*65*, *66*), JSBACH-SPITFIRE (*67*), JULES-INFERNO (*68*), CTEM fire module (*69*, *70*), and MC-Fire (*71*). For FireMIP, all of the modeling groups completed simulations with a standardized set of input variables (*34*). A transient run was performed by all modeling groups, with some groups also performing sensitivity simulations where population density or landcover remained constant at year 1700 values.

The complexity of the models in FireMIP varied widely (*34*, *59*), including empirical as well as process-based models, with different representation of the human impact on global fire occurrence (see Table S3). Most FireMIP models included human ignitions, and the typical non-linear response function for modeled human ignition increases with growing population at low population densities before saturating or declining at high population densities to reflect fire suppression efforts. In addition, four models explicitly accounted for human suppression on fire spread/burned area, also as a function of population density (CLM fire module, LPJ-GUESS-SIMFIRE-BLAZE, JSBACH-SPITFIRE, and CTEM fire module). CLM was the only model that accounted for the influence of economic development (static GDP) on fire spatial patterns (Table S3). The representation of vegetation and fuels in FireMIP models depends on the underlying ecosystem model (mostly dynamic global vegetation models) and the treatment of land use in each model. Most models assume that fire does not occur in croplands, while land cover conversion from forest to pasture may increase burned area. However, only the CLM fire module explicitly included fire-driven deforestation (Table S3). MC-Fire, JULES-INFERNO and LPJ-GUESS included vegetation responses to climate that altered vegetation type and fuels; in all other models, vegetation composition changes over time were only due to land use change. The MC-Fire model allowed plants to adapt to fire, such that burned area declines over time in frequently-burning areas as the modeled vegetation supports less fire activity.

Given the different characteristics of both the underlying ecosystem models and fire models, differences in modeled trends over the study period may be expected, even with common driver data for climate, population and land use. Increasing population in many parts of the world may increase or suppress modeled burned area, depending on tradeoffs between ignitions and suppression as determined by the parameterization of population effects in the various models. The treatment of land use in each model may also cause different trends. For instance, models differed in the way that natural vegetation was transformed for agricultural use and whether land cover accounting tracked net or gross transitions between land cover types. While all models exclude croplands from burning, most models estimated an increase in burned area in pasture areas (Table S3).

Based on the FireMIP sensitivity simulations, we explored how changing population density and land use contributed to changes in modeled burned area over the study period (Table S4). Because sensitivity runs were not

available for all models, we also investigated the spatial patterns of modeled and observed burned area from all models to characterize burned area responses to climate, vegetation, and socio-economic differences (Fig. S14). Although processes of land use expansion were well represented within the models, influences of land use intensification or increasing investment per unit of agricultural area were not yet accounted for (Table S3, Fig. S15). Using the data on the number and size of modeled fires from the three SPITFIRE models (Table S5), we explored the importance of landscape fragmentation and fire characteristics for modeled burned area trends.

The spatial relationship between land use activity and burned area

We evaluated the relationship between land use and fire activity using regional spatial correlations between burned area and (a) population density, (b) cropland area, and (c) livestock density (Fig. 4). For global population we used estimates from the 2013 Gridded Landscan population dataset developed by US Department of Energy, Oak Ridge National Laboratory (*72*, *73*). For livestock density, we used global gridded livestock data for 2007 from the Food and Agricultural Organization (*74*). We used tropical livestock units (TLU) to combine cattle (TLU=0.7), goats (TLU=0.1) and sheep (TLU=0.1) densities into a single map of livestock density (*75*). Finally, we assessed the fraction of cropland in each grid cell using the MODIS MCD12Q1 (collection 5) land cover product from 2001 (*76*). All three datasets were rescaled to a 0.25° spatial resolution. The sub-grid cell spatial correlation (Pearson's r) between mean annual burned area (GFED4s, 1998 – 2015) and human land use (population density, cropland fraction, and livestock density) was calculated at 1.5° spatial resolution from all 0.25° pixels within each larger 1.5° grid cell (N = 36, and excluding water pixels). Finally, we calculated the mean correlation per fractional tree cover bin based on the MODIS vegetation continuous fields (MOD44B collection 5, *58*), mean correlation was calculated for each 5% tree cover bin, including all grid cells with greater than 50% vegetation cover and mean annual burned area greater than 1% yr^{-1}.

Country-level trends in burned area and agriculture

We also considered country-scale trends in burned area and agricultural activity (Fig. S11). For each country, we estimated annual burned area trends from GFED4s data, while annual trends in the fraction of the country used for agriculture and gross agricultural output value (an indicator of productivity) were derived from annual country-level time series retrieved from the FAO data portal (*77*). The FAO data was only available through 2013, limiting the study period to 1998 – 2013.

We analyzed the 51 countries with most annual burned area. This set accounted for more than 98% of global burned area and each of these countries had a total amount of burned area that exceeded about 1 Mha yr^{-1}. Countries were divided into three groups (n=17) based on changes in the fraction of land used for agriculture. Group 1, which collectively had a decline, or small increase in agricultural area included Australia, Botswana, Canada, Central African Republic, China, Colombia, Congo, Democratic Republic of the Congo, India, Mexico, Mongolia, Namibia, Russia, South Africa, Ukraine, United States and Venezuela. Group 2 which collectively had a medium increase in agricultural area included Angola, Bolivia, Brazil, Cameroon, Chad, Kazakhstan, Kenya, Laos, Madagascar, Mali, Mozambique, Myanmar, Nigeria, Senegal, Sudan, Thailand and Zambia. Group 3 which collectively had a large increase in agricultural area, included Argentina, Benin, Burkina Faso, Cambodia, Ivory Coast, Ethiopia, Ghana, Guinea, Indonesia, Malawi, Paraguay, Sierra Leone, Togo, Uganda, Tanzania, Vietnam and Zimbabwe. For each group, we calculated mean trends in (a) fraction of agricultural area, (b) gross agricultural output, and (c) burned area to compare the burned area response to changes in agricultural activity.

Land and fire use transition

We developed a conceptual model of changes in burned area as a function of land management and socio-economic development (Fig. 5). The model was derived from spatial patterns of population density, gross domestic product (GDP), land use, and burned area for humid (Fig. S12, precipitation ≥ 1200 mm yr^{-1}) and semi-arid (Fig. S13, 500 – 1200 mm yr^{-1}) regions in the tropics and subtropics (40°N – 40°S). Land cover type was estimated using the MODIS MCD12Q1 (collection 5) land cover product from 2001 (*76*). The original land cover types in the University of Maryland classification were aggregated into three land cover classes: closed canopy forest (including all forests), open canopy plant function types (including all other land cover types except croplands), and croplands. MCD64A1 burned area at 500-m spatial resolution was divided among "closed canopy", "open canopy" and "cropland." The combination of MODIS land cover and burned area in large fires (≥21 ha) attributes fires to specific cover types at 500-m resolution. However, MODIS resolution may not capture small fires in deforestation or agricultural areas (*26*), resulting in an underestimate of fire activity during certain stages of the "fire use transition" shown in Fig. S12 and S13 where small fires are prevalent. Gridded Landscan population data for 2013 (*72*, *73*) and country-level data on per capita GDP for 2013 (*77*) were combined to estimate the product of population and per capita GDP, with

units of \$ km^{-2} yr^{-1}. We refer to the product of population and per capita GDP as GDP-density. All datasets were rescaled to a 0.25° spatial resolution.

We investigated the impact of socio-economic development on land use and burned area for different regions by creating equal sized bins of 0.25° grid cells (5% per bin) of increasing GDP-density, and studying the distribution of land cover types and burned area per land cover type for each bin. Common lands are shaped by indigenous fire use, with extensive burning in savannas and grasslands and infrequent fire use in forests. Today such conditions mostly persist in national parks and indigenous reserves in the Americas (*78*) and remote areas of Africa and Australia. In building our conceptual model, we assumed that grid cells with GDP-density below \$1000 km^{-2} yr^{-1} were representative of such common land management conditions. These grid cells represent areas with a near absence of people in developed countries, or sparsely populated rural areas in developing countries. Between GDP-densities of \$1000 km^{-2} yr^{-1} and \$20,000 km^{-2} yr^{-1}, land cover and fire use changed rapidly, described as the "transition" phase in the conceptual model. After this initial transition, changes were more gradual with increasing GDP-density. Because of data limitations, Fig. S12 and S13 only show the transition until \$100,000 km^{-2} yr^{-1}, which is equal to a low population density in more developed countries, and would be comparable to "low capitalization" in the conceptual model shown in the main text. Our conceptual model for fires as a function of development and land use transition stage builds upon the classic environmental analyses of *Hardin* (*79*) and *Foley et al.* (*31*).

Earth system impacts of declining burned area

We evaluated the impact of declining burned area on vegetation dynamics, carbon cycling, and air quality using time series of ancillary satellite data and model results (Fig. S4, S16, S17 and Table S6). We used two different vegetation indices to explore the relationship between trends in burned area and changes in vegetation cover (Fig. S16). From MODIS we used the enhanced vegetation index (EVI, MCD13C2 collection 6, global). From TRMM we used the vegetation optical depth (VOD) time series (*80*, 50°N – 50°S). We estimated the spatial correlation between trends of each of these products and trends in burned area over the period when both products were available (2001 – 2014). EVI is primarily sensitive to vegetation greenness and green leaf area while VOD is sensitive to vegetation water content; combined, EVI and VOD provide information on changes in vegetation structure (*47*, *49*). We focused on dry season changes in vegetation indices and estimated trends in both datasets using values during the month with lowest mean annual precipitation (2001 – 2014). In most regions, the driest month did not correspond to the peak fire month (*81*), reducing the direct effect of fire on vegetation index values. Dry season values also increased the sensitivity of our analysis to changes in woody vegetation, given differences in senescence between herbaceous vegetation and deeper rooted woody vegetation during the dry season (*49*, *82*). We calculated the correlation (Pearson's r) between the trends in vegetation indices and burned area for all frequently burning grid cells (with mean burned area ≥10 % yr^{-1}) in South America, Africa, Australia and the world (Table S6).

We used the GFED modeling framework to quantify the impact of declining burned area on the global carbon cycle (Fig. S17). The GFED model is based on the Carnegie-Ames-Stanford-Approach (*27*, *42*, *83*). We ran two model simulations, one with the observed GFED4s burned area time series (1997 – 2015) and one with GFED4s burned area for 1997 – 2001 followed by a climatological mean annual cycle of burned area 2002 – 2015 that was derived from data during 1997 – 2001. Both model simulations had the same spin-up and parameter set. For this analysis, we focused on the increase in land carbon storage (Fig. S17) from declining burned area in grasslands and savannas in the tropics and mid-latitudes (40°N – 40°S).

We used absorption aerosol optical depth (aAOD, MIL3MAE) from the Multi-angle Imaging Spectroradiometer (*84*, MISR) to characterize the impact of declining burned area on atmospheric aerosol concentrations (Fig. S4b). In addition, we analyzed surface CO concentrations from the Measurements Of Pollution In The Troposphere (MOPITT) instrument version 7, after correcting for a bias drift of -0.59 % yr^{-1} (*85*, Fig. S4c). To minimize the effects of concurrent changes in non-fire aerosol and CO sources, we limited our analysis to trends in aAOD and CO during the month of peak burning. We calculated the spatial correlation (Pearson's r) between trends in burned area (GFED4s) and trends in aAOD and CO (all 2003 – 2015) for frequently burning grid cells (mean annual burned area ≥10 % yr^{-1}, mostly located in the tropics) for the world, South America, Africa, and Australia (Table S6).

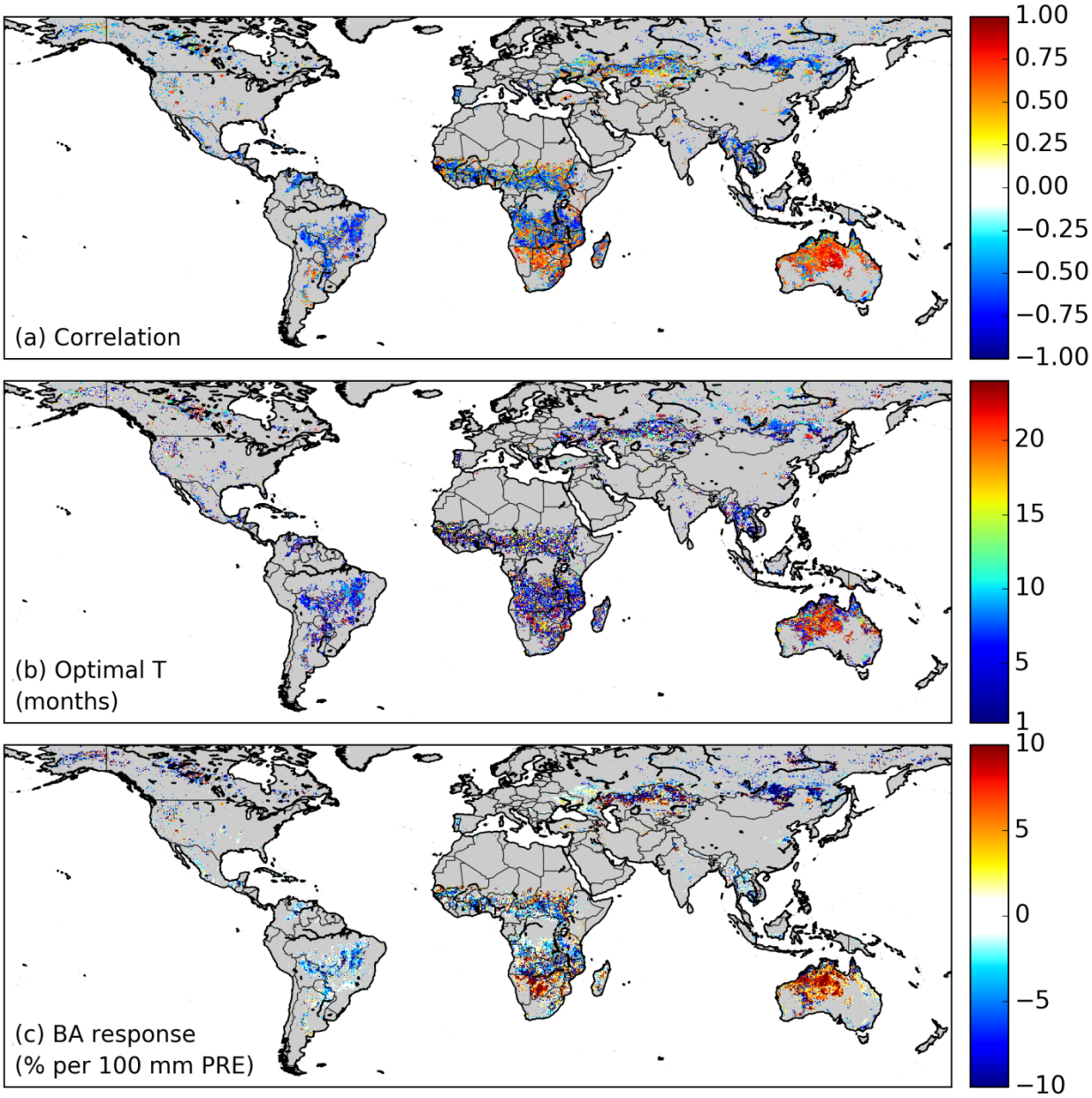

Fig. S1: Global patterns of burned area response to precipitation. (a) The largest absolute (positive or negative) correlation between inter-annual variability in antecedent precipitation and burned area. Positive correlations captured the role of antecedent precipitation for fuel build up in arid ecosystems, while negative correlations were observed in more humid savannas and tropical forest regions where fuel moisture during the dry season limited fire activity. (b) The precipitation lead time (*T*, eq. 1) for the largest absolute correlation shown in (a). Regions with negative correlations between burned area and precipitation typically had shorter lead times, as higher fuel humidity suppressed fire activity, whereas xeric ecosystems with a positive precipitation response exhibited longer lead times (i.e., the fuel buildup effect). (c) Estimated response of burned area (% of grid cell burned) to a 100 mm positive anomaly in precipitation (PRE) based on the MCD64A1 data. The modeled burned area response was the absolute response, and thus depended on the typical amount of biomass burning as well as the impact of precipitation. Regions of infrequent burning (i.e. grid cells with mean burned area <1 % yr^{-1}) are masked in gray.

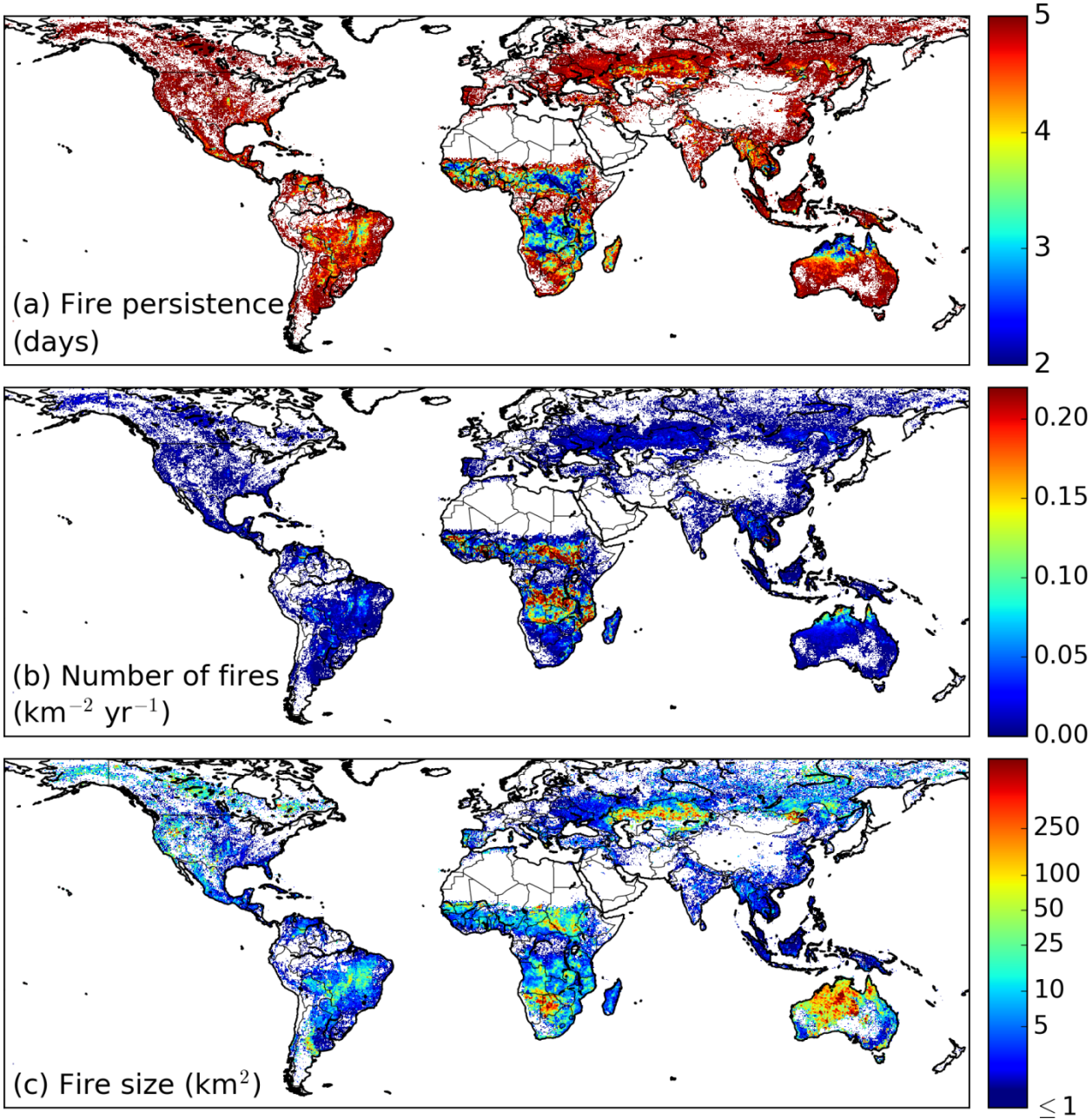

Fig. S2: Demographics of fire activity during 2003-2015 based on individual large fires (≥21 ha) from MCD64A1 burned area. (a) Mean fire persistence for each grid cell (0.25°), showing the upper threshold (in days) for assigning neighboring 500-m grid cells to the same fire event. (b) Mean annual number of fires (km^{-2} yr^{-1}) and (c) mean fire size (km^2), weighted by the burned area of the individual fires. We found the highest density of ignitions in the humid tropical savannas, with up to 0.2 fire events km^{-2} yr^{-1} in Africa. On average, the largest fires occurred in more arid grasslands and savannas in southern Africa, the Asian steppe, and Australia.

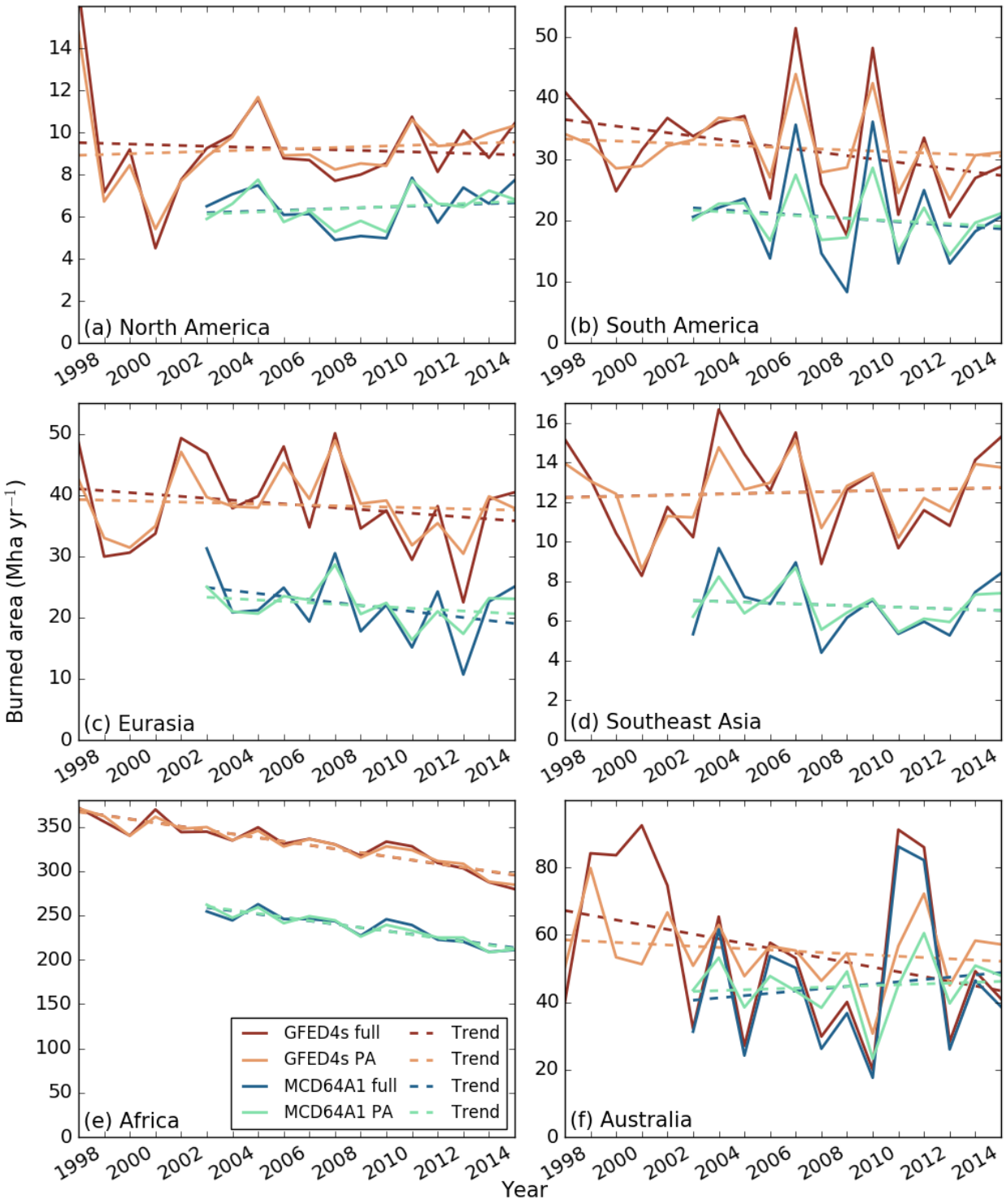

Fig. S3: Continental trends in GFED4s (1998 – 2015) and MCD64A1 (2003 – 2015) burned area. Panels indicate time series and linear trends for the full and precipitation adjusted (PA) burned area time series. For most regions, declines in burned area were consistent between datasets over the different time intervals, with the exception of Australia and Southeast Asia, where burned area during 1997 – 2001 was strongly influenced by El Niño Southern Oscillation. Accounting for the influence of precipitation strongly reduced the variance in burned area trends, although some strong regional climate anomalies still influence the PA burned area time series (e.g., the 2007 and 2010 droughts in parts of South America). Several studies have shown that a non-linear model may be needed to capture extremes in fire activity in response to drought conditions for tropical forest regions (*86–88*).

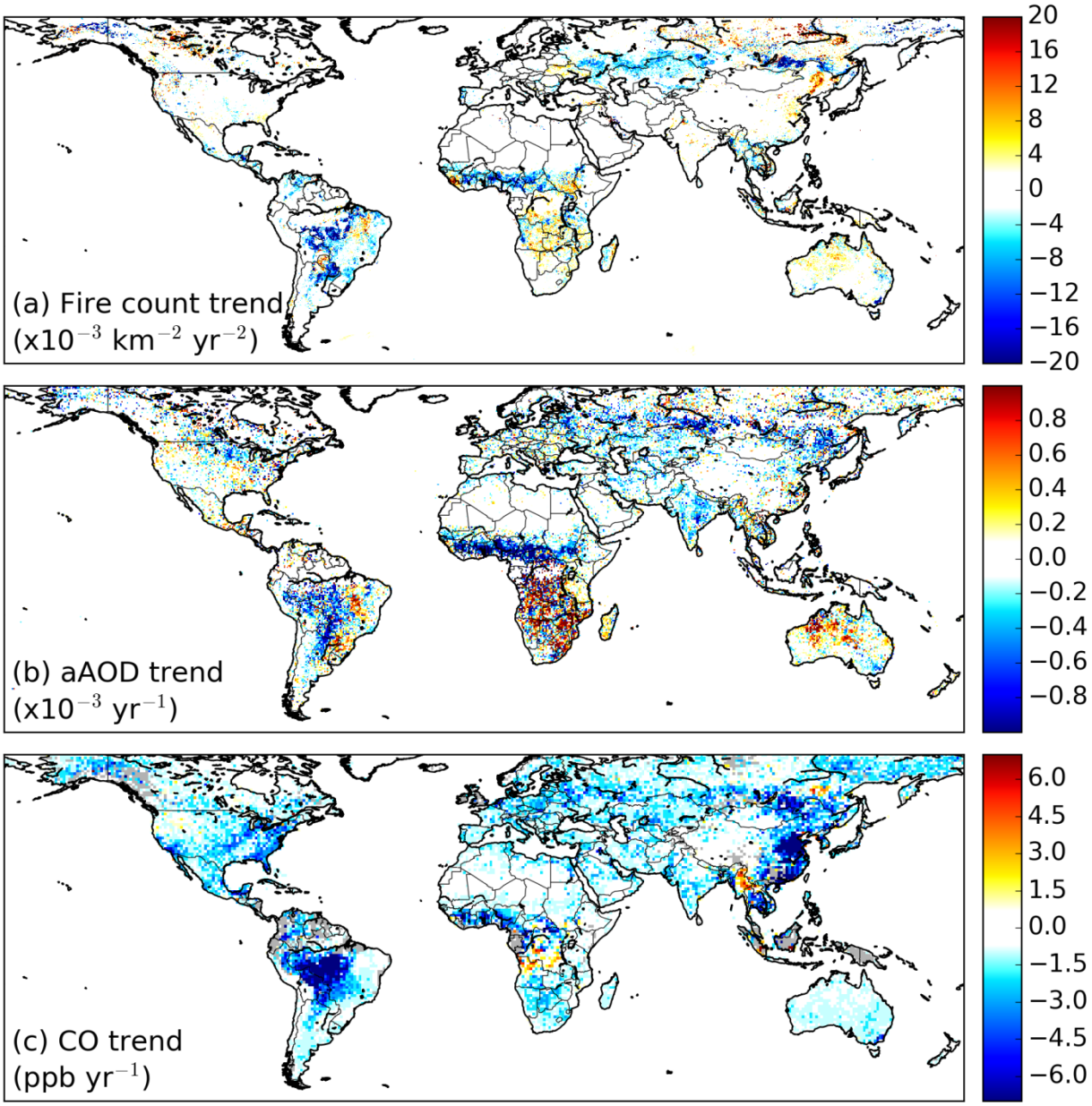

Fig. S4: Trends in active fire detections, aerosols, and surface CO concentrations were similar to the spatial distribution of trends in burned area during 2003 – 2015. (a) Trends in MODIS (Terra and Aqua) fire counts per fire season, (b) trends in MISR aerosol absorption optical depth (aAOD) during the peak burning month, and (c) trends in MOPITT surface CO concentrations during the peak burning month. MOPITT CO data were not available during months of persistent cloud cover and trends were not calculated for grid cells with fewer than 8 out of 13 years of valid data (these areas are masked gray). Declining burned area in South America, Asia, and northern Africa resulted in lower aerosol and surface CO concentrations during the burning season, with regional impacts on air quality and climate. In general, aAOD trends showed stronger agreement with trends in biomass burning in more xeric ecosystems, while CO trends showed better agreement for more humid ecosystems, characterized by more incomplete combustion and high fuel consumption. Declining CO concentrations were also observed over several densely populated industrial regions (e.g., the east coast of the US and China). The trends in active fire detections provided independent evidence of spatial patterns of global decline in biomass burning over the study period.

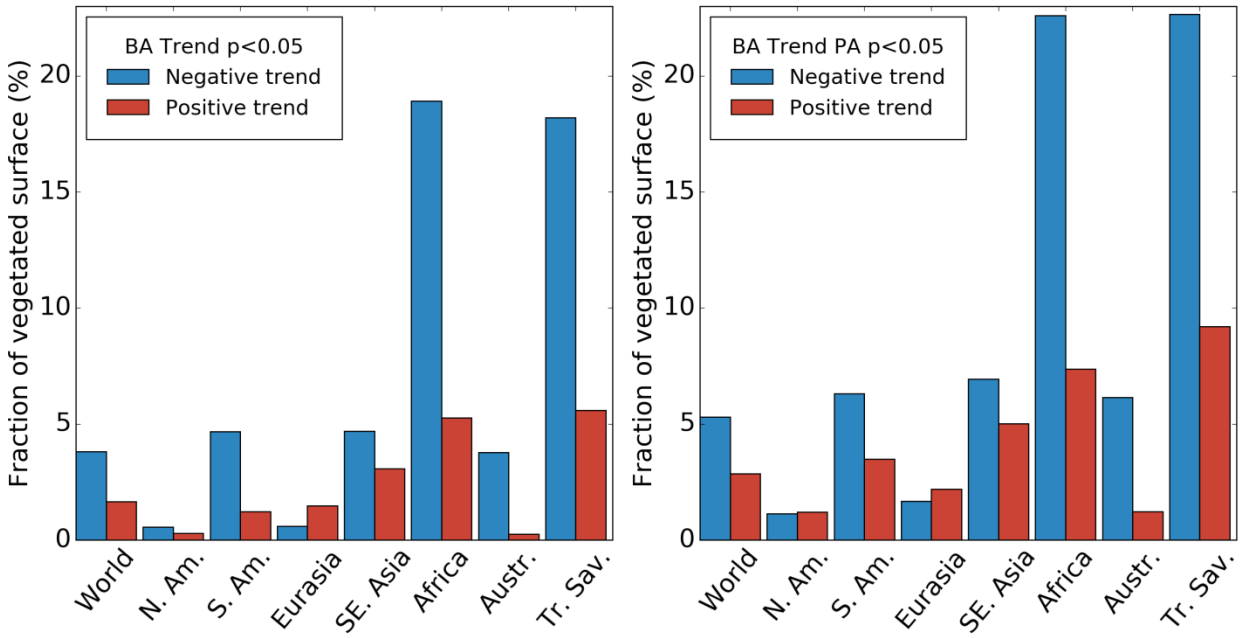

Fig. S5: The fraction of grid cells with a significant decrease in burned area was larger than the fraction with significant increases for all regions except Eurasia (GFED4s burned area, 1998 – 2015). Panel (a) shows the land surface fractions with significant ($p<0.05$) trends in the full burned area times series and panel (b) shows significant precipitation-adjusted (PA) trends in burned area as a fraction of the land surface in different regions. After controlling for inter-annual variability in precipitation, about 8.2% of the vegetated surface experienced significant changes burned area (a 5.3% decrease and a 2.9% increase). Focusing on tropical grasslands and savannas (Tr. Sav., all 0.25° grid cells between 23°N – 23°S with land cover ≥50% grassland, savanna or woody savanna combined), 22.7% of grid cells showed a significant decrease compared to 9.2% with a significant increasing trend in burned area over the study period. Trends in grid cells with less than 1% mean annual burned area were excluded from this analysis.

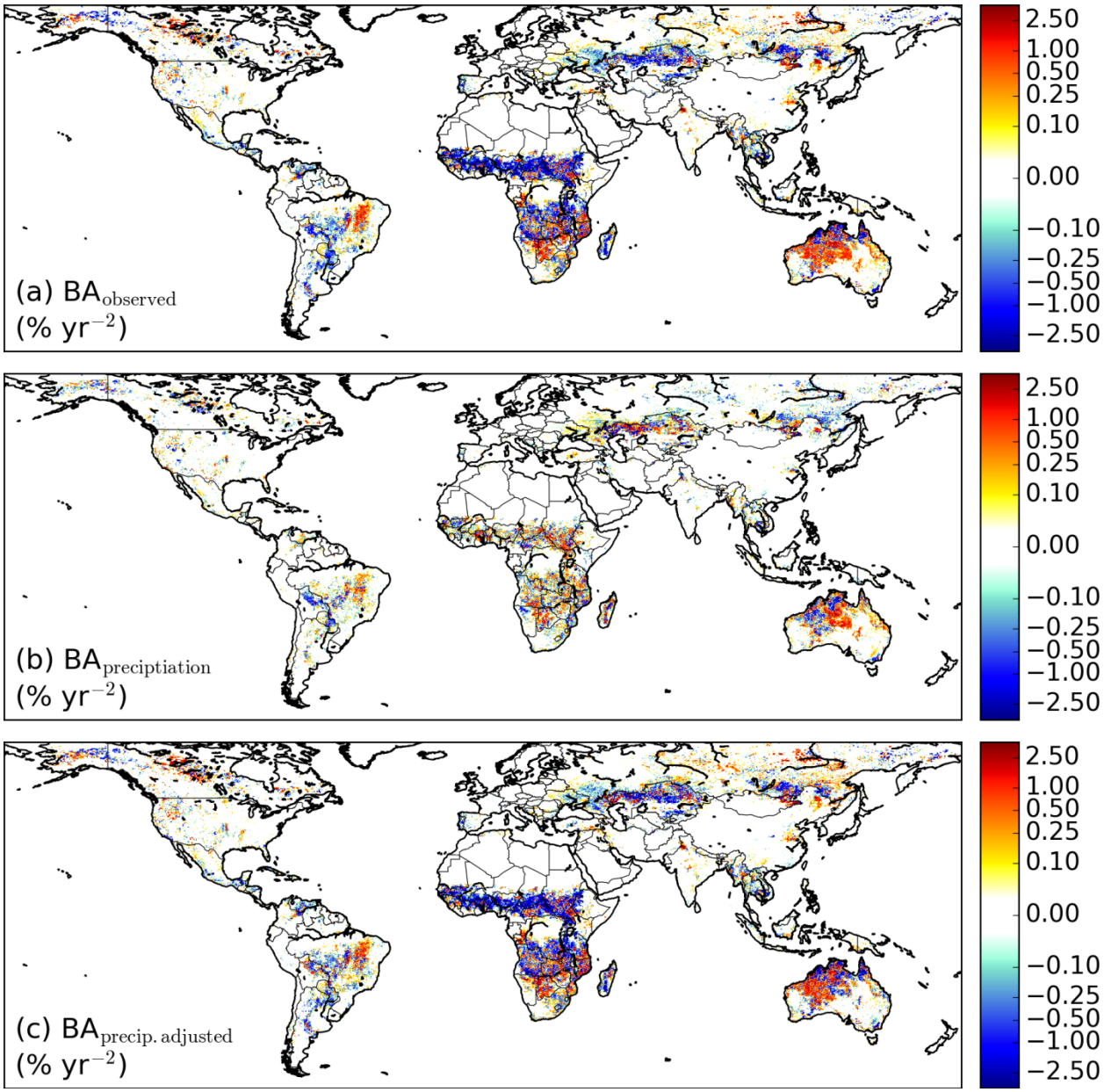

Fig. S6: Precipitation is an important driver of inter-annual variability in burned area but cannot explain the sign or magnitude of burned area trends for many regions. Trends in (a) observed burned area ($BA_{observed}$) from the MCD64A1 burned area data (2003 – 2015). (b) Precipitation-induced trends in burned area ($BA_{precipitation}$) for this time series, and (c) Precipitation adjusted trends in burned area ($BA_{precip.\ adjusted}$, or BA_{PA}). Precipitation trends were consistent with increasing burned area in central Australia, arid regions of southern Africa, and the Brazilian Cerrado. In other regions, however, the precipitation-induced trends in burned area were low, or even had the opposite sign of the observed trends, for example in northern Africa and the Asian steppe.

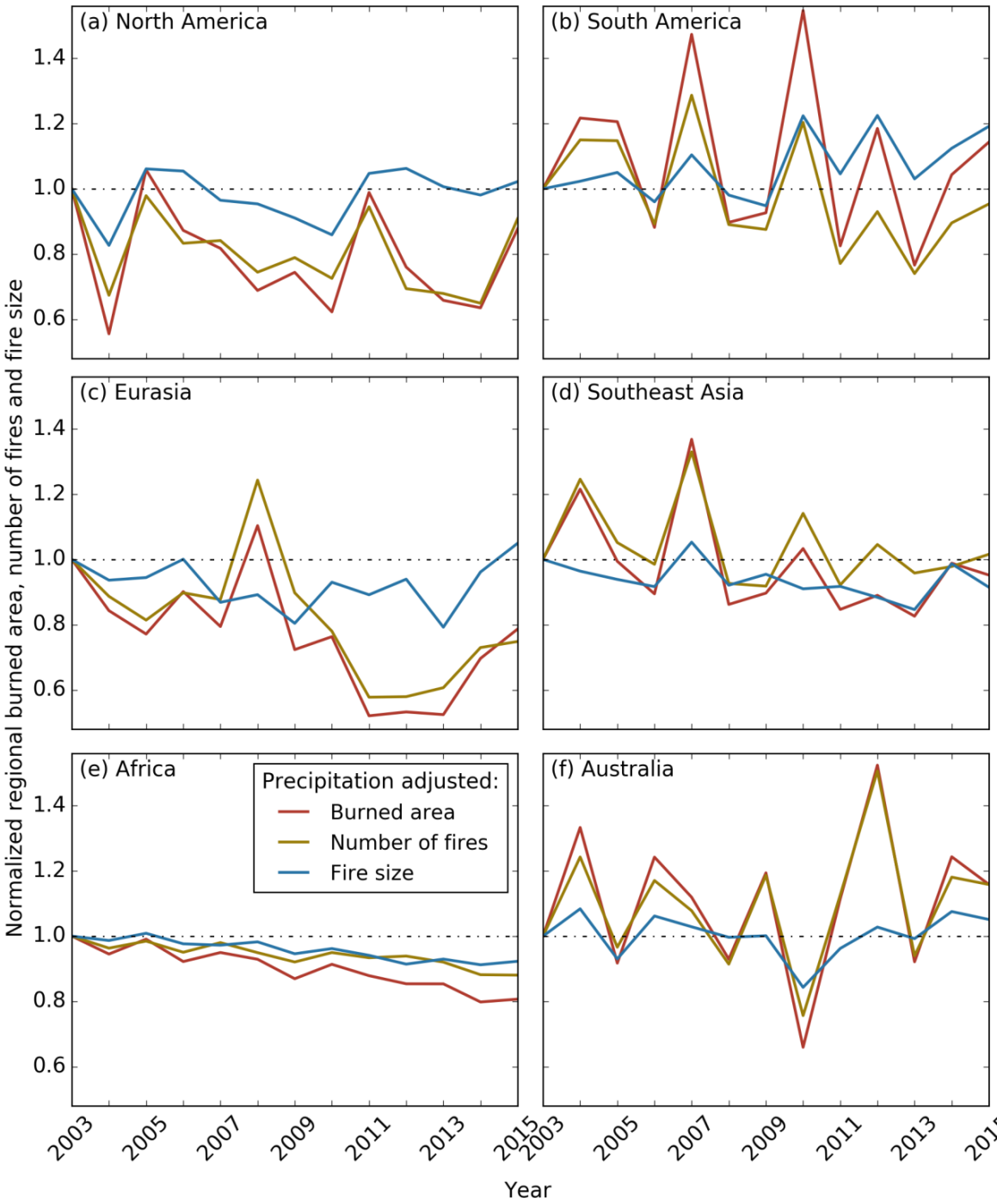

Fig. S7: Regional time series of burned area, number of fires, and fire size after controlling for precipitation-induced variation: (a) North America, (b) South America, (c) Eurasia, (d) Southeast Asia, (e) Africa, and (f) Australia. For all of the time series, we normalized the different fire properties by dividing by 2003 values. For each year, burned area is the product of the number of fires and fire size, highlighting the relative contributions from the number and size of fires to burned area trends by continent. Infrequently burning clusters of grid cells (burned area below 5 km^2 yr^{-1}) were excluded from this analysis, excluding about 6% of global annual burned area, mostly in the arid subtropics and boreal forests. In South America, a small increase in mean fire size mostly canceled the negative trend associated with decreasing fire number. In Eurasia, the observed decline in burned area was mostly driven by a lower number of fires. In Africa, the number and size of fires both steadily declined, resulting in a strong decrease in burned area. For sub-regional trends, see Table S1.

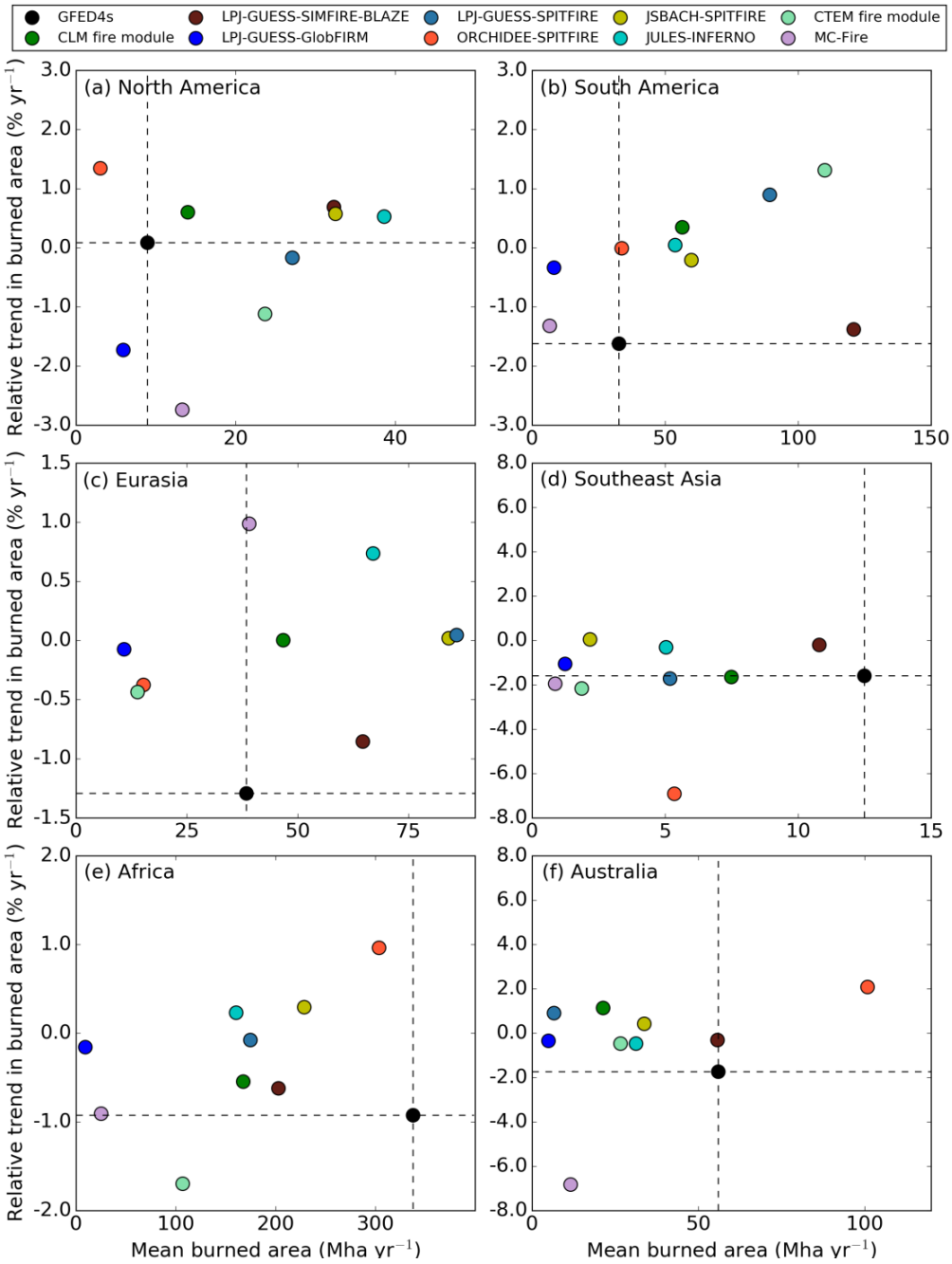

Fig. S8: Continental comparison of mean annual burned area and relative burned area trends from GFED4s with the FireMIP models for: (a) North America, (b) South America, (c) Eurasia, (d) Southeast Asia, (e) Africa and (f) Australia. FireMIP model estimates were available from 1997 – 2013 for six models, from 1997 – 2012 for the CTEM fire module and JULES-INFERNO, and from 1997 – 2009 for MC-Fire. Trends for additional subcontinental-scale regions are presented in Table S2 and Fig. S10. GFED4s observations are shown in black and the model estimates in different colors. In general, FireMIP models overestimated burned area in the Americas and underestimated burned area in Africa, Australia, and Southeast Asia, although model estimates varied widely. Similarly, while some models predicted a global scale decline in burned area (Fig. 3), the spatial distribution of modeled trends differed from observations. Modeled relative trends were often accompanied by large differences in estimates of absolute burned area, with little agreement among models. The largest disagreements between modeled and observed trends in burned area were found in South America and Eurasia, two regions with rapid transitions in fire use as a consequence of changing patterns of land use.

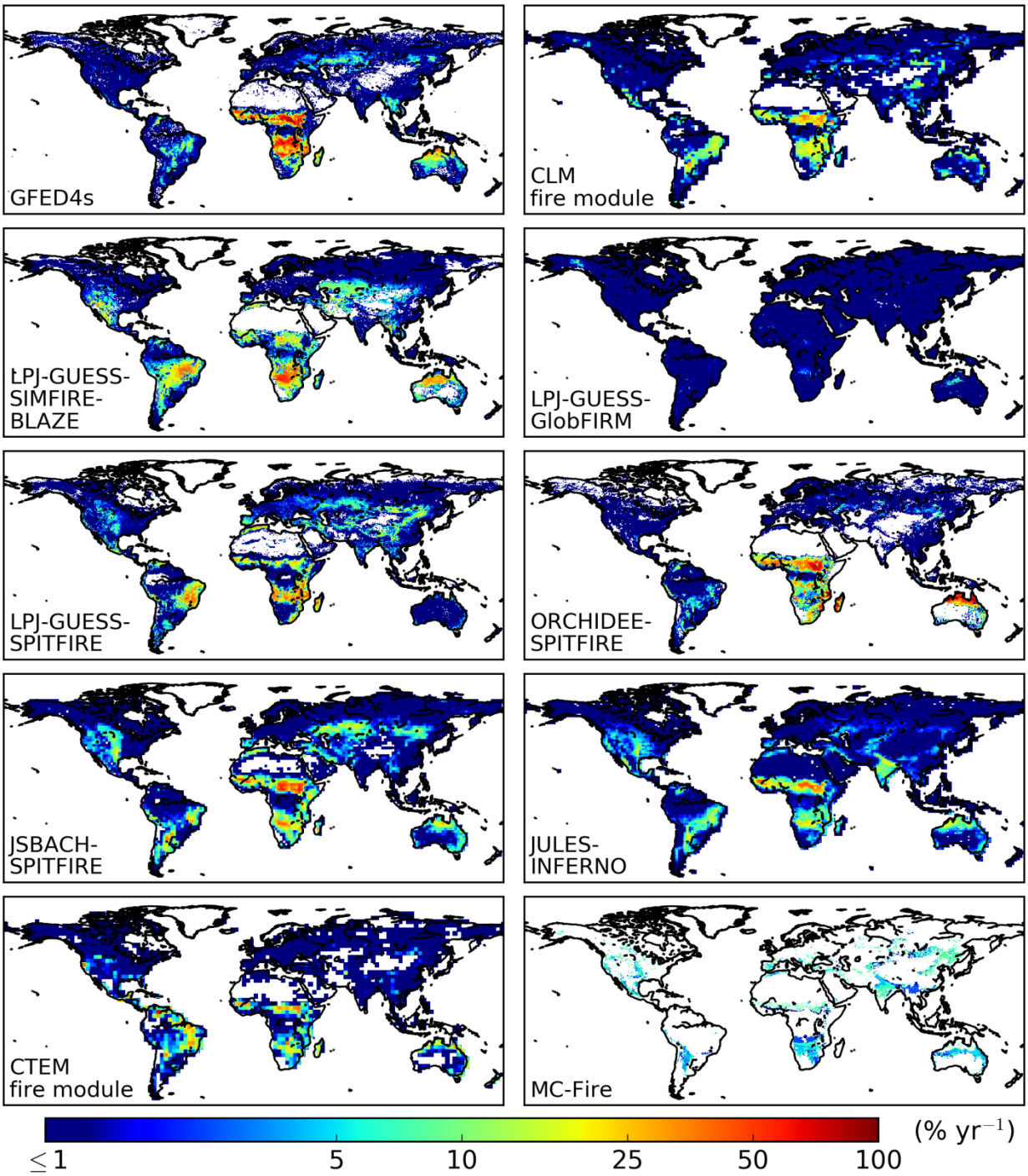

Fig. S9: Mean annual burned area estimated by GFED4s and FireMIP models. FireMIP data were available from 1997 – 2013 for all models except the CTEM fire module and JULES-INFERNO (both 1997 – 2012) and MC-Fire (1997 – 2009). Most models captured the spatial pattern of global mean annual burned as estimated by GFED4s, although several models overestimate fire activity in the Americas and underestimate burned area in Africa and Australia. In addition, most models underestimated burned area in humid tropical regions, while LPJ-GUESS-GlobFirm and MC-Fire considerably underestimated global burned area in general. Areas without observed or modeled burned area are shown in white.

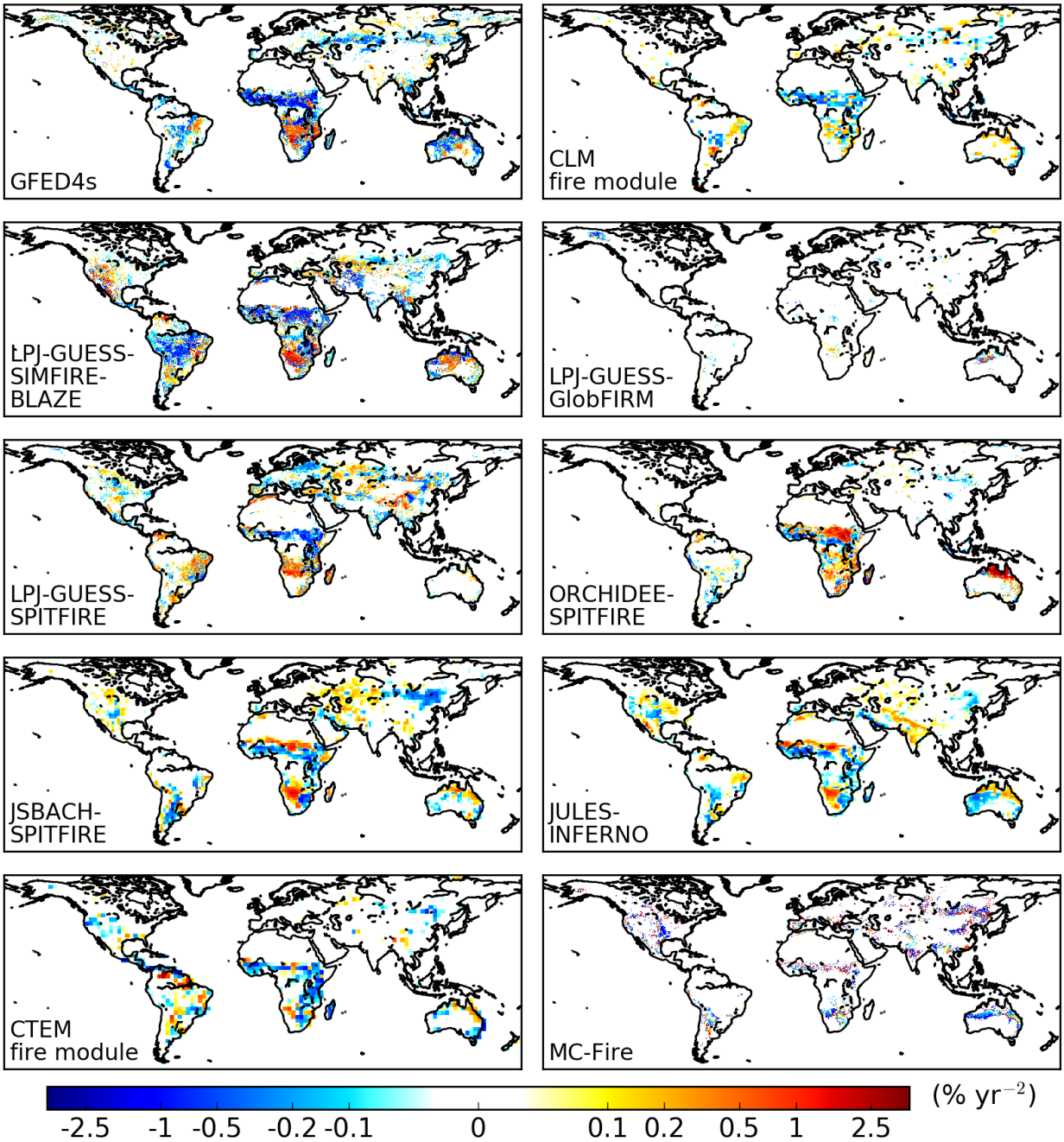

Fig. S10: Trends in annual burned area estimated by GFED4s and FireMIP models (1997 – 2013). FireMIP data were available from 1997 – 2013 for all models except the CTEM fire module and JULES-INFERNO (both 1997 – 2012) and MC-Fire (1997 – 2009). Most models captured the decline in burned area for humid savannas in northern Africa, but modeled decreases were offset in many models by increasing burning in semi-arid and arid regions. Model estimates varied widely for South America, while none of the models captured the observed magnitude of the burned area decline in central Asian grasslands.

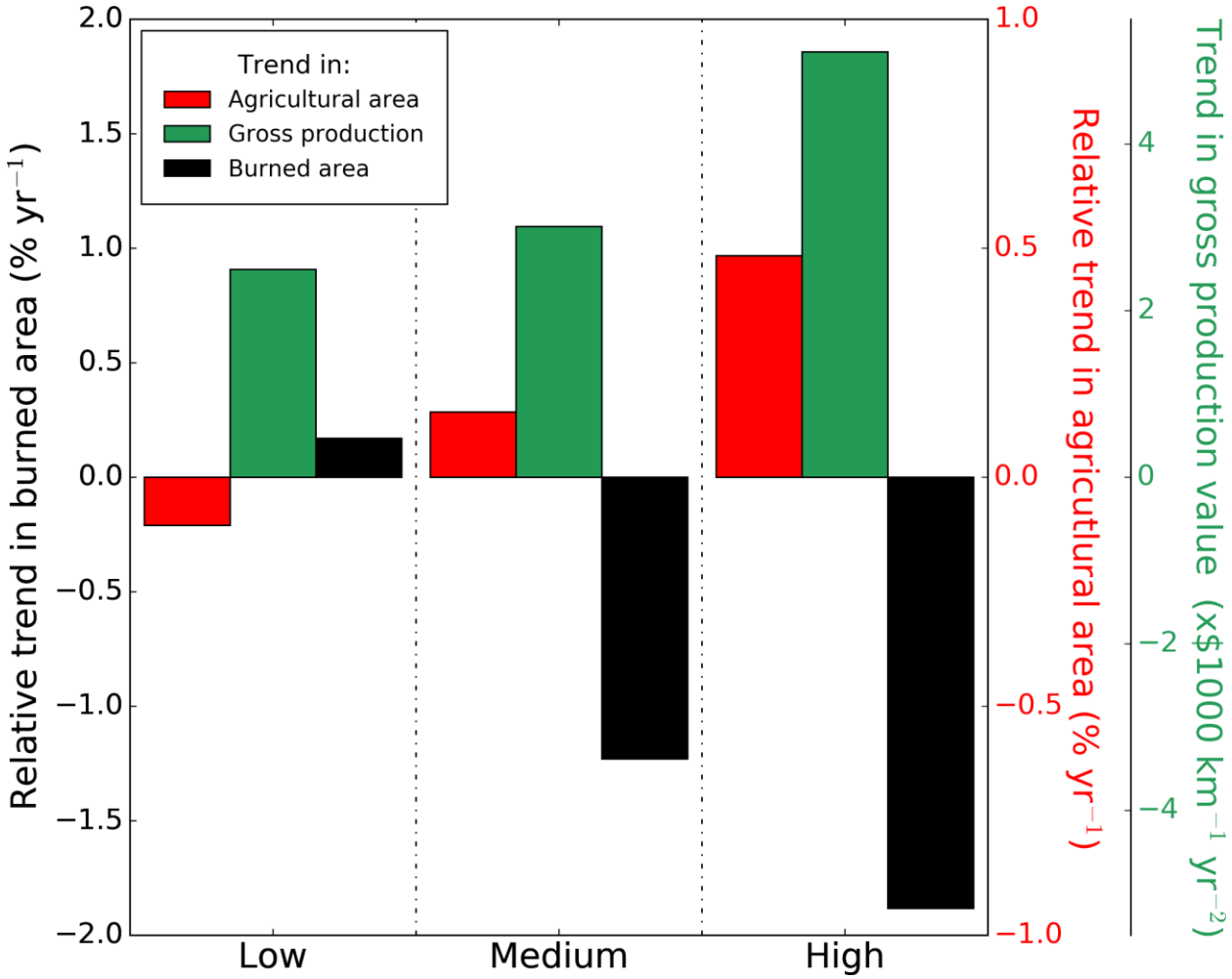

Fig. S11: Countries with the largest relative increases in agricultural area and production value had the greatest relative declines in burned area during 1998 – 2013 (GFED4s, precipitation adjusted). The 51 countries that account for >98% of global burned area were grouped in three equal bins (low, medium, high, n=17 for each bin) according to the relative trends in agricultural area between 1998 – 2013. The mean trend in gross production value provides an indication of increasing agricultural capitalization during this period for each group of countries.

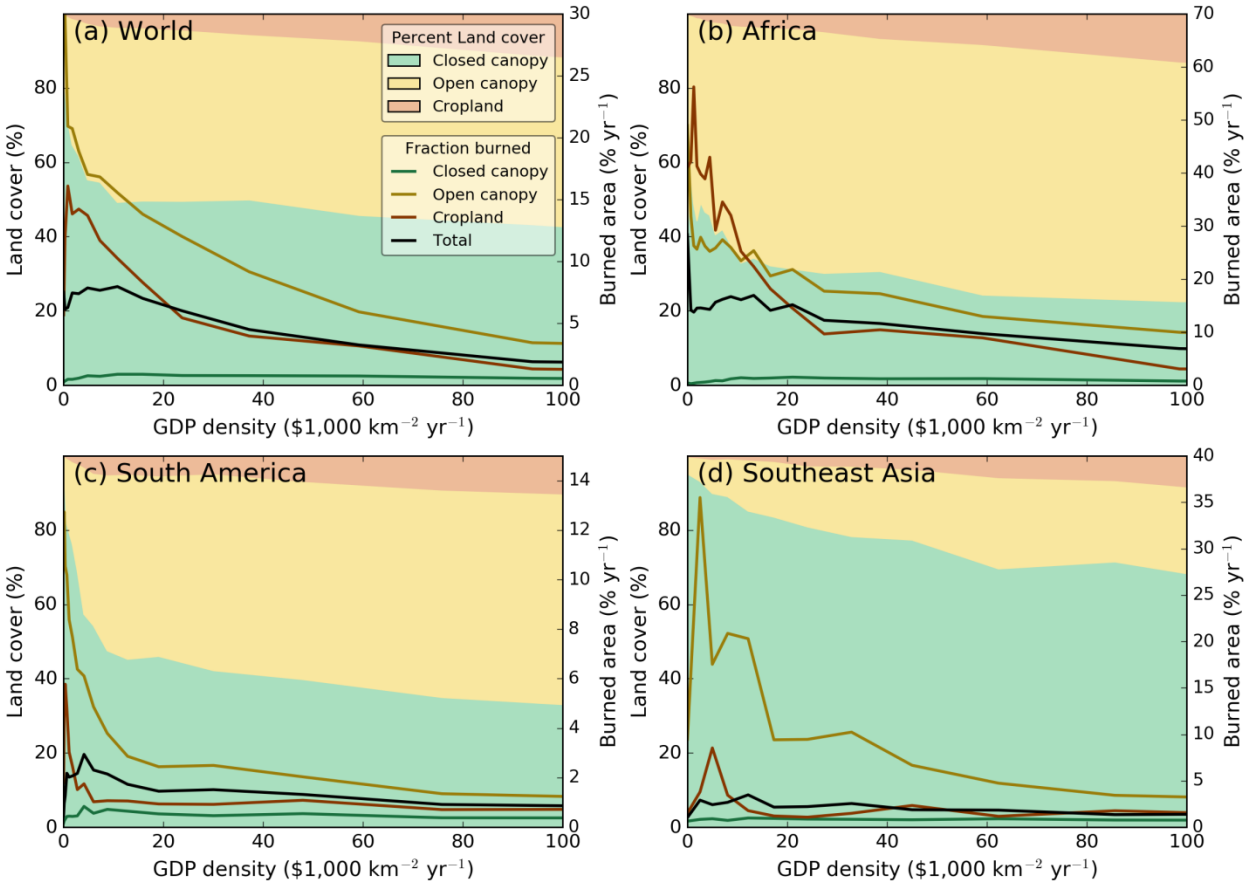

Fig. S12: Burned area changes in predictable ways with increasing GDP density across the humid tropics and subtropics. Land cover and mean burned area per land cover type (MCD64A1, 2003 – 2015) are shown as a function of GDP density (national per capita GDP distributed over the landscape using gridded population data) for humid regions: (a) the world, (b) Africa, (c) South America and (d) Southeast Asia. Colored surfaces indicate the distribution of land cover (left y-axis) and colored lines track the fraction of burned area for each land cover type (right y-axis). The solid black line (Total) indicates mean annual burned area for all cover types. Although the absolute burned area varied by continent, all regions had an initial increase in fire activity, driven by land cover conversion and increased fire activity in tropical forests, followed by a decline in total burned area as fractional cropland area and development increased.

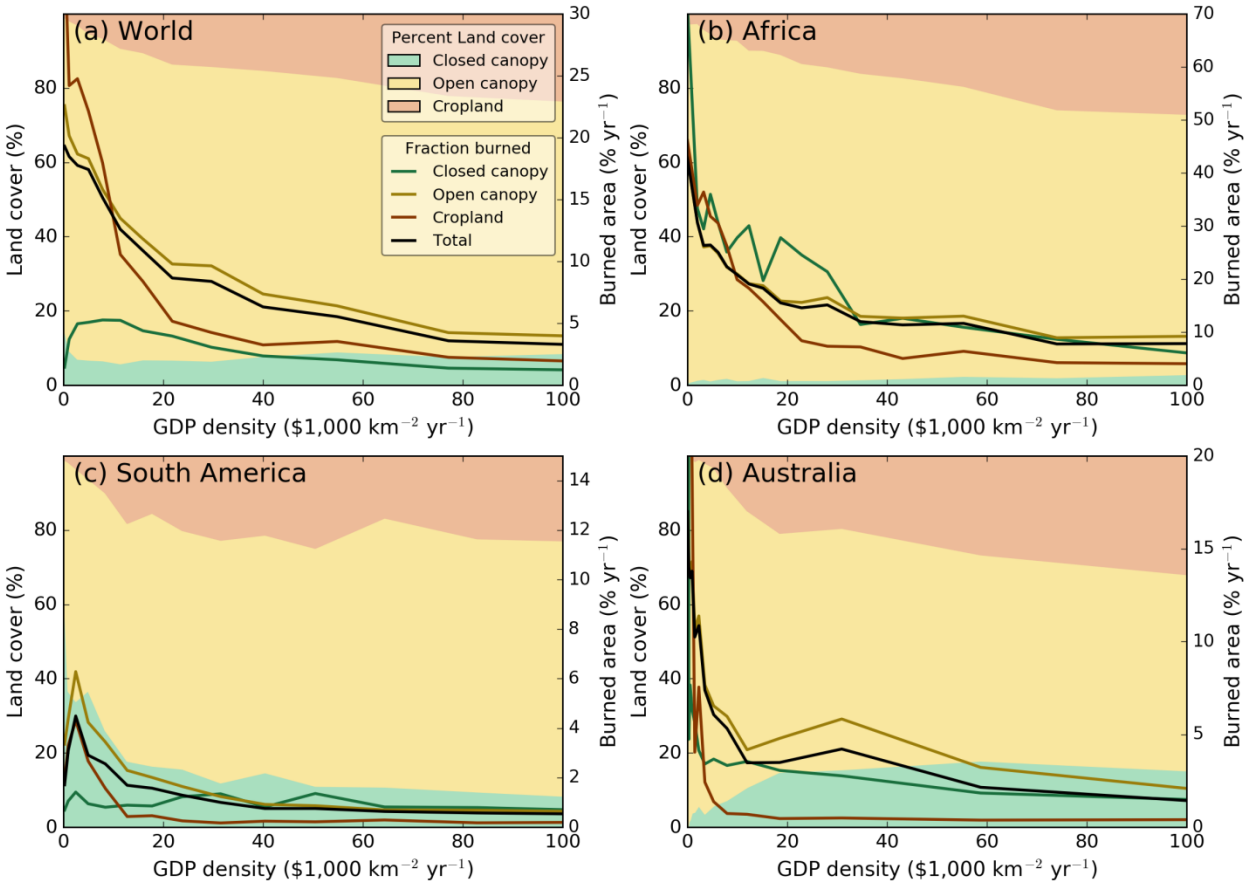

Fig. S13: Same as Fig. S12, but for semi-arid regions: (a) the world, (b) Africa, (c) South America and (d) Australia. Semi-arid regions of the tropics and subtropics exhibited non-linear declines in total burned area following land cover conversion for cropland. Patterns of land development and burned area differ between semi-arid regions and the humid tropics, as semi-arid savannas and grasslands supported high levels of burning at low population densities. With increasing cropland extent and livestock density, fewer and smaller fires in more fragmented landscapes led to a rapid decline in burned area, even at low levels of capitalization.

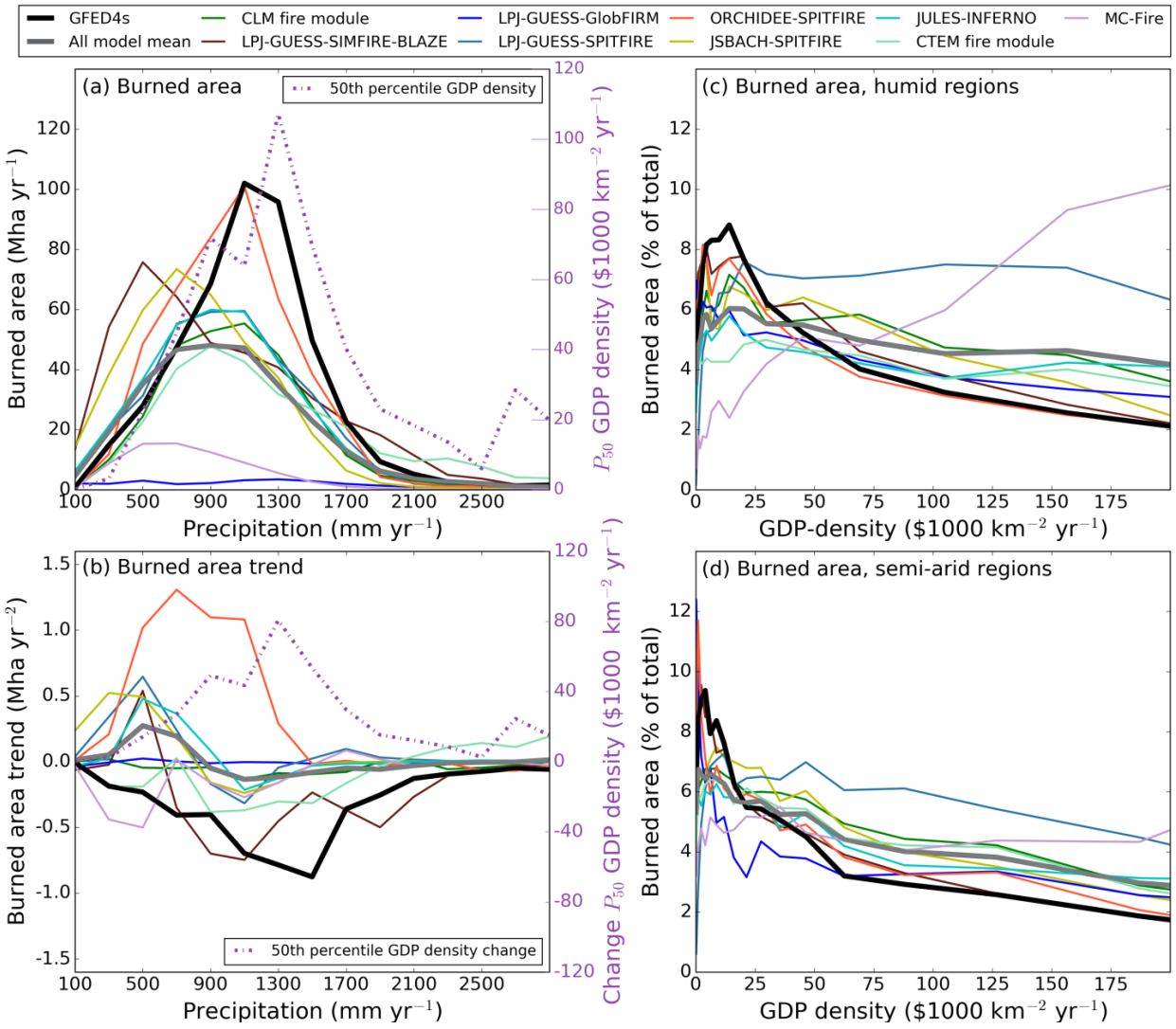

Fig. S14: Comparison of observed and modeled estimates of burned area as a function of precipitation and GDP density for all land 40°N – 40°S. (a) Distribution of GFED4s and FireMIP estimates of mean annual burned area averaged within 200 mm yr^{-1} increments of precipitation. (b) Same as (a) but comparing burned area trends during 1997 – 2013. In panels a and b, the 50th percentile (P_{50}) of GDP density and GDP density change are plotted in a purple dotted line on the right y-axis. (c) Distribution of GFED4s and FireMIP estimates of mean annual burned area as a function of GDP density for humid ecosystems (with unevenly spaced bins, each containing 5% of the total number of grid cells). (d) Same as (c) but for semi-arid ecosystems. In all panels, GFED4s observations are shown in black, the models estimates are shown with colors and the all model mean estimate is shown in gray. Peak burned area in most models occurred in more arid ecosystems (700 – 1100 mm yr^{-1}) than peak burned area in the satellite observations (1100 – 1300 mm yr^{-1}). The underestimate of modeled burned area in productive savannas likely contributed to differences between modeled and observed burned area trends because of more rapid socio-economic development in these ecosystems, which was quantified here using changes in GDP density in panel b. Model responses to rising atmospheric CO_2 may have contributed to greater fuel availability in arid regions, where many models not only overestimated burned area but also exhibited a positive trend in fire activity. Panels c and d are similar to the theoretical model of burned area change as a function of increasing GDP-density (Fig. 5, S12 and S13). FireMIP models underestimated declines in burned area with rising capitalization for both humid and semi-arid ecosystems for GDP densities higher than $50,000 km^{-2} yr^{-1}. In humid regions, the models also underestimated increases in burned area at very low levels of capitalization, between $5000 and $20,000 km^{-2} yr^{-1}. This latter bias suggests the models underestimated fire use at the deforestation frontier in tropical forests.

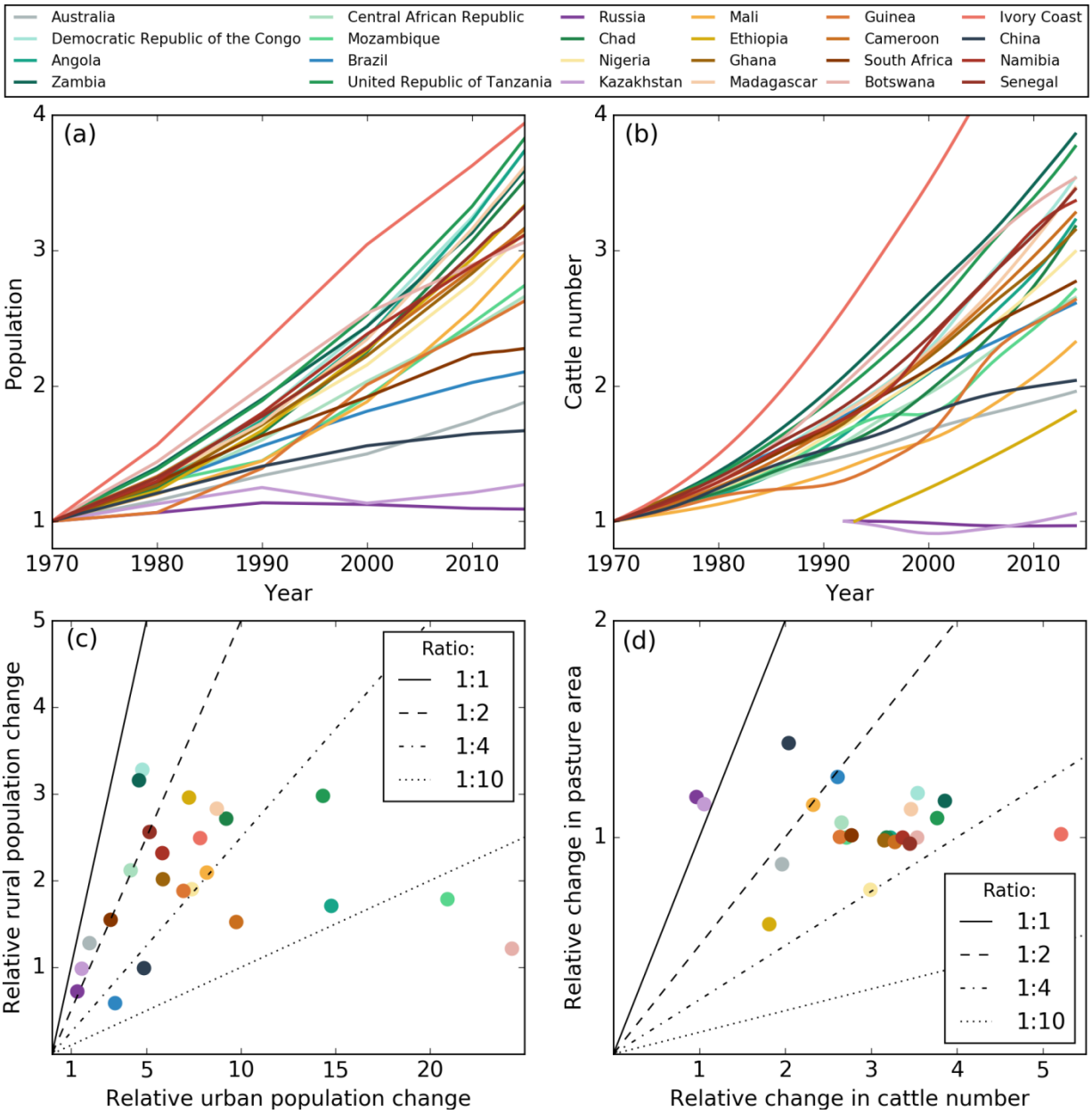

Fig. S15: Human population and cattle number have risen exponentially since 1970 in the 24 countries with the greatest amount of burned area, driven by strong trends towards urbanization and increasing stocking density. Per country relative changes in (a) population and (b) cattle between 1970 – 2015. (c) Population changes in most countries were driven by rapid urbanization, with between two and ten times more urban residents in 2015 compared to 1970. (d) Cattle stocking densities doubled or tripled since 1970, while pasture area remained relatively constant, especially for African countries. In all subplots (a-d), values for each country were normalized to 1970 (1970 = 1) with the exception of Russia, Kazakhstan, and Ethiopia where data were available after 1992 (1992 = 1). Population statistics and pasture area were obtained from the HYDE 3.1 dataset (*89*), and data on cattle were downloaded from the FAO data portal (*77*). Rapid transformation of population demographics and agricultural intensification likely contributed to observed declines in burned area, yet these factors were not included in FireMIP models. Differentiation between rural and urban population growth may help refine estimates of human ignition and suppression in fire models. Similarly, accounting for livestock density may reduce fuel load and fuel continuity in models that include fires for pasture management (Table S3).

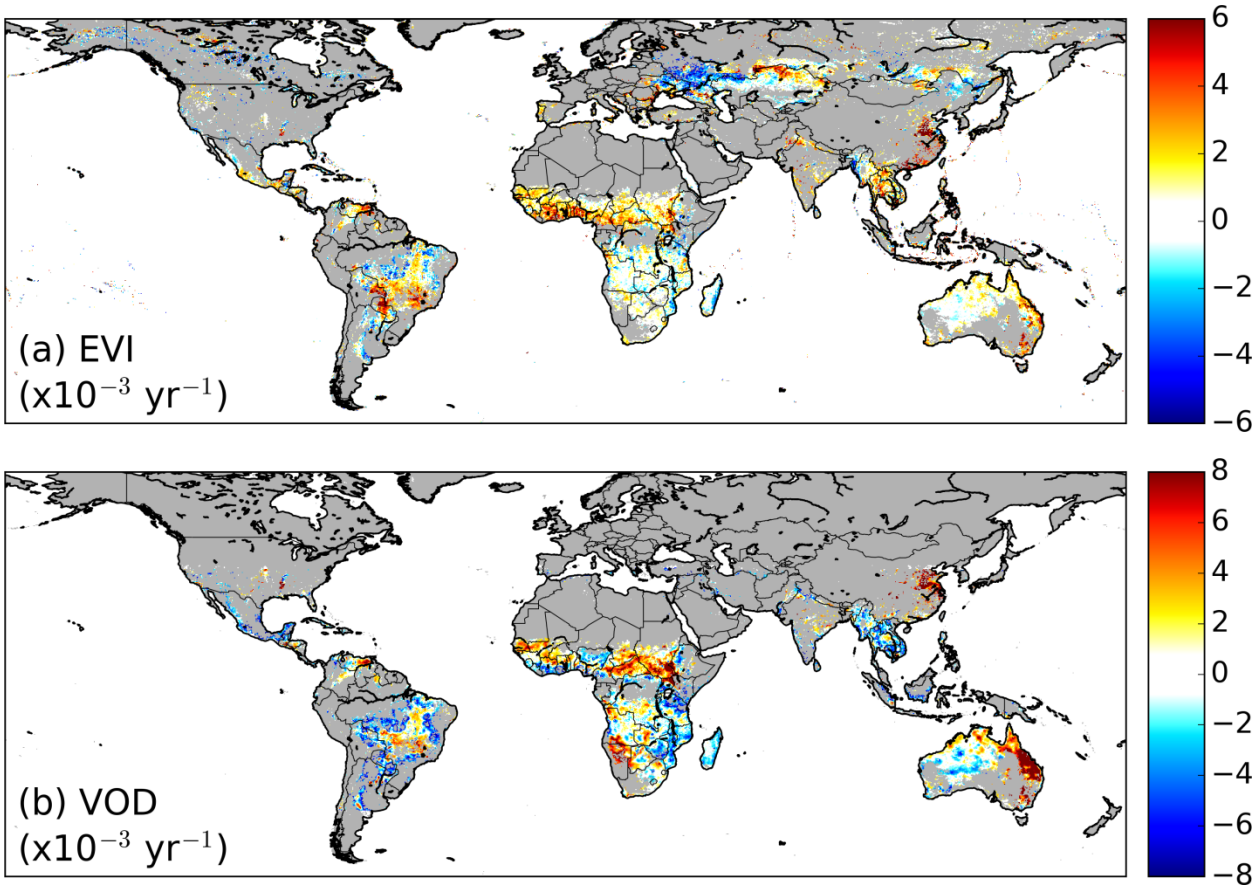

Fig. S16: Time series of satellite data provided evidence for increases in vegetation productivity and moisture content in regions with declining burned area trends across the tropics. (a) Dry season trends in the enhanced vegetation index (EVI) and (b) vegetation optical depth (VOD) for 2001 – 2014. Grid cells with burned area below 1% yr^{-1} are masked gray and VOD data are only available from 50°N to 50°S. Spatial correlation between burned area trends and EVI trends was strongest in Africa and South America (see Table S6), where declining burned area led to increases in vegetation greenness. Spatial correlation between burned area trends and VOD trends provided evidence for two different forms of land cover change. In South America, declining fire activity following land cover conversion yielded a persistent decline in VOD, which is consistent with a loss of forest and shrub cover in agricultural ecosystems. Declining fire activity in Australia and Africa, in contrast, yielded increases in VOD, consistent with higher moisture content and/or increases in woody vegetation.

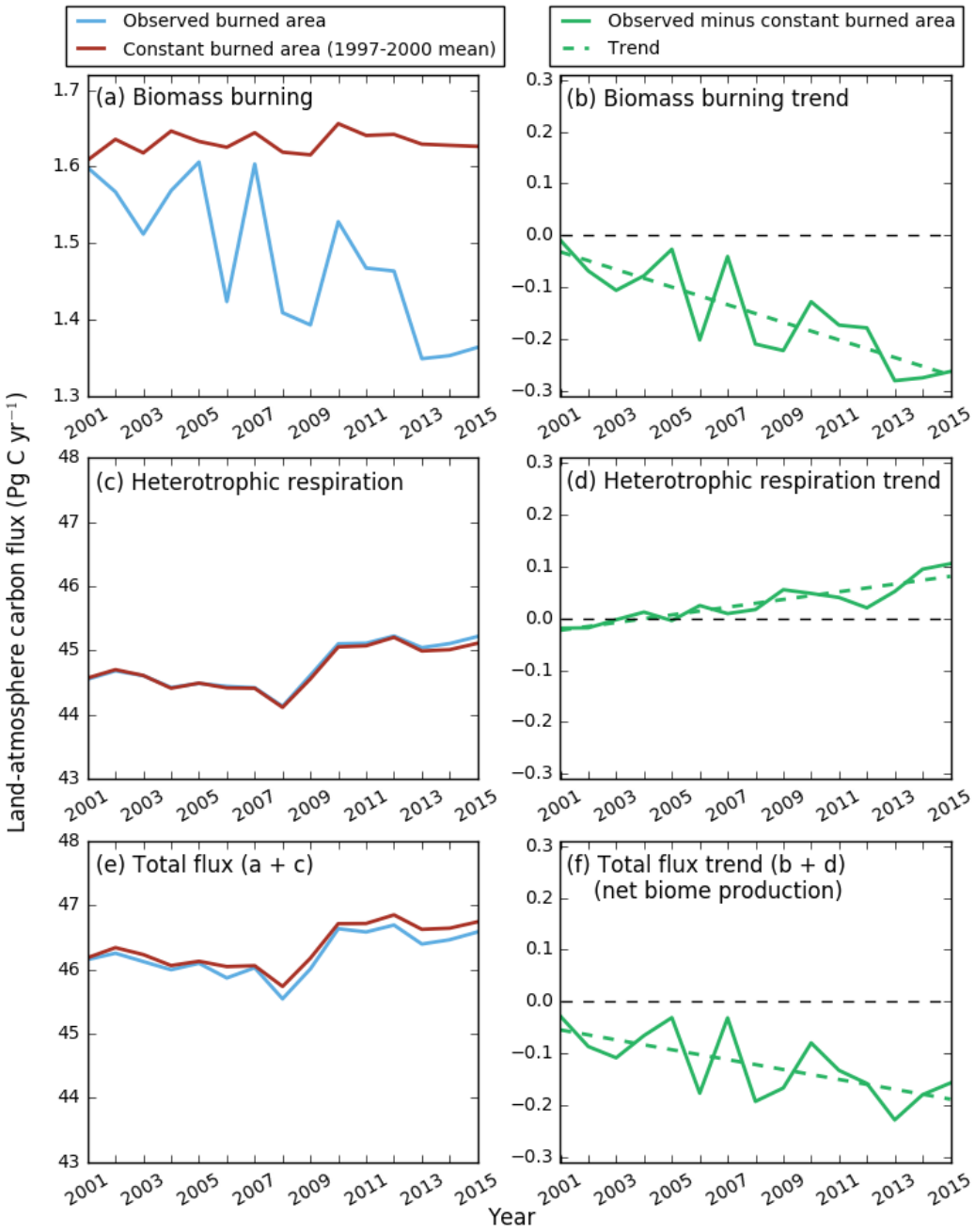

Fig. S17: Modeled increase in land carbon storage from declining burned area in tropical and subtropical grasslands and savannas between 2001 and 2015. The impact of declining burned area was estimated using the difference between model simulations with observed (blue) and constant burned area (red) following the same model spin-up and observed burned area through 2001. By 2015, fire emissions with observed burned area from GFED4s were nearly 0.3 Pg C yr^{-1} lower than the scenario with constant burned area (a,b). The observed decline in burned area led to an increase in heterotrophic respiration, partially offsetting some of the increase in vegetation carbon storage from declining fire activity (c,d). However, because respiration is a slower process than fire, declining burned area in tropical and subtropical grasslands and savannas generated a land sink of 0.2 Pg C yr^{-1} by 2015 (e,f). Our estimate of the carbon sink from declining fire activity was likely conservative because declining fire activity did not change the fractional abundance of woody vegetation within the model and burned area declines were only modeled from 2001 onwards.

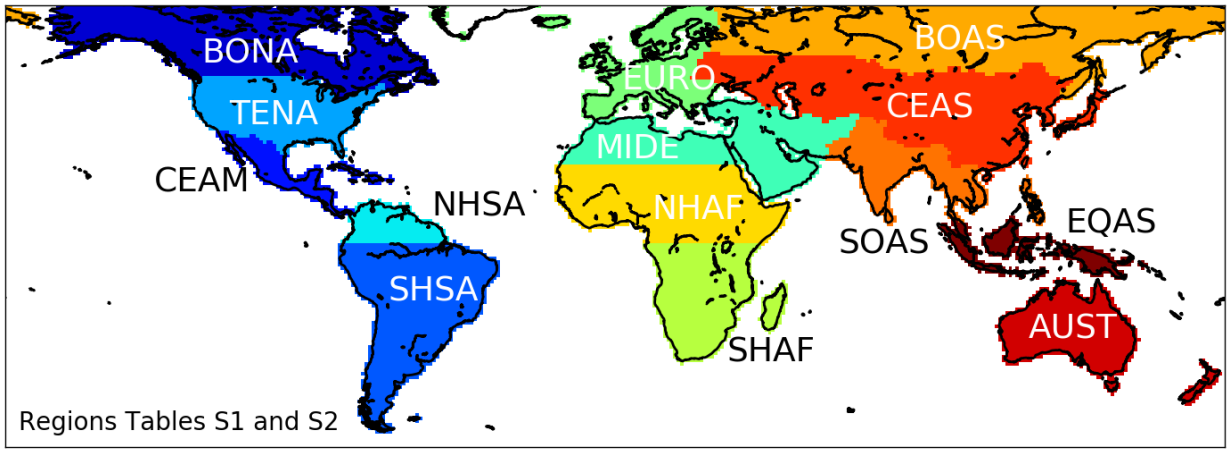

Fig. S18: Map of GFED regions used to summarize observed and modeled trends in tables S1 and S2. Regional abbreviations: boreal North America (BONA), temperate North America (TENA), Central America (CEAM), northern hemisphere South America (NHSA), southern hemisphere South America (SHSA), Europe (EURO), Middle East (MIDE), northern hemisphere Africa (NHAF), southern hemisphere Africa (SHAF), boreal Asia (BOAS), Central Asia (CEAS) southern Asia (SOAS), equatorial Asia (EQAS), and Australia and New Zealand (AUST).

Table S1: Relative trends in burned area, number of fires, and mean fire size for the GFED regions (Fig. S18). Trends are shown for different time periods, as indicated, to directly compare burned area estimates from different sources. All trends were calculated using per fire season estimates of burned area except FireMIP data that were produced and analyzed per calendar year. Colors indicate increases (red) and decreases (blue) in burned area for each region and time period; significant trends are denoted by asterisks (* p<0.1, ** p<0.05, and *** p<0.01).

Fire product	Time period	Full or residual[1]	Trend (% yr^{-1}) with 95% confidence limits														
			World	BONA	TENA	CEAM	NHSA	SHSA	EURO	MIDE	NHAF	SHAF	BOAS	CEAS	SOAS	EQAS	AUST
Burned area (GFED4s)	1998-2015	Full	-1.35 (0.49)***	2.68 (4.73)	1.41 (2.47)	-4.32 (4.79)*	-1.57 (1.93)	-1.70 (3.19)	-4.17 (3.71)**	0.46 (2.73)	-2.30 (0.29)***	-0.35 (0.63)	-1.78 (4.65)	-1.05 (2.59)	1.02 (1.70)	1.36 (5.95)	-2.56 (4.26)
		PA	-0.99 (0.29)***	3.99 (3.76)**	2.03 (2.10)*	-3.89 (3.53)**	-1.56 (1.35)**	-0.30 (1.95)	-4.24 (2.92)***	0.52 (1.69)	-2.25 (0.26)***	-0.37 (0.49)	-0.39 (2.75)	-0.72 (1.89)	1.05 (1.19)*	1.11 (3.93)	-0.69 (1.92)
Burned area (GFED4s) during the MODIS era	2003-2015	Full	-1.27 (0.95)**	2.97 (7.54)	0.23 (3.95)	-3.34 (4.78)	-3.29 (3.32)*	-2.53 (6.23)	-4.72 (3.66)**	2.16 (4.34)	-2.84 (0.42)***	-0.38 (0.91)	-3.78 (8.52)	-2.75 (3.76)	0.52 (2.59)	1.64 (10.13)	1.49 (8.01)
		PA	-1.17 (0.39)***	3.98 (5.62)	0.95 (3.55)	-3.85 (3.18)**	-3.19 (2.05)***	-1.47 (3.66)	-4.62 (2.51)***	1.75 (2.96)	-2.69 (0.37)***	-0.39 (0.70)	-1.02 (4.94)	-2.25 (2.77)	0.66 (1.65)	1.71 (6.73)	0.38 (3.16)
Burned area from 500m MODIS MCD64A1	2003-2015	Full	-1.15 (1.21)*	3.14 (7.84)	1.53 (5.94)	-4.72 (7.02)	-2.70 (5.06)	-1.20 (7.89)	-6.41 (6.74)*	3.67 (5.30)	-3.05 (0.71)***	-0.36 (0.98)	-2.03 (11.11)	-3.70 (5.01)	0.52 (3.21)	2.37 (12.47)	1.54 (8.26)
		PA	-1.23 (0.44)***	3.85 (5.30)	1.49 (5.13)	-5.25 (4.60)**	-3.30 (2.62)**	-0.75 (4.23)	-5.48 (4.16)**	3.11 (2.83)**	-3.17 (0.52)***	-0.39 (0.70)	1.35 (6.22)	-3.31 (3.29)**	0.61 (1.78)	2.57 (7.68)	0.55 (3.41)
Fire number	2003-2015	Full	-0.98 (0.73)**	6.58 (14.65)	0.67 (3.01)	-3.97 (4.32)*	-2.16 (3.32)	-2.77 (5.91)	-3.70 (5.24)	2.72 (4.04)	-1.81 (0.57)***	-0.08 (0.55)	-8.70 (14.94)	-4.47 (4.93)*	-0.34 (2.86)	2.43 (7.24)	1.51 (6.72)
		PA	-1.00 (0.35)***	9.73 (10.00)*	0.26 (2.67)	-3.97 (2.83)**	-2.26 (1.62)**	-2.10 (3.14)	-3.01 (4.29)	2.66 (2.99)*	-1.85 (0.40)***	-0.07 (0.39)	-7.27 (9.04)	-4.87 (3.72)**	-0.23 (1.63)	1.75 (3.79)	0.71 (2.88)
Fire size	2003-2015	Full	-0.39 (0.38)**	0.69 (2.81)	1.82 (2.52)	-1.72 (2.10)*	-1.27 (2.04)	1.79 (2.21)	-2.55 (2.91)*	0.60 (1.76)	-1.23 (0.43)***	-0.36 (0.34)**	2.18 (1.56)**	-0.38 (2.79)	0.32 (1.08)	0.07 (2.86)	-0.28 (1.66)
		PA	-0.43 (0.18)***	2.16 (2.84)	1.26 (1.64)	-1.76 (1.46)**	-1.51 (1.38)**	1.66 (1.24)**	-1.22 (2.23)	0.79 (1.23)	-1.34 (0.32)***	-0.33 (0.23)***	2.59 (1.66)***	-0.68 (1.85)	0.25 (0.81)	-0.21 (1.51)	0.09 (1.10)
Burned area predicted by FireMIP[2]	1997-2013	Full	-0.13 (0.56)	-0.33 (1.76)	-0.16 (1.44)	0.23 (1.11)	1.50 (1.42)	-0.27 (0.71)	0.58 (1.81)	0.44 (1.18)	-1.09 (1.33)	0.19 (0.85)	-0.00 (0.91)	0.09 (1.03)	-0.68 (1.16)	-5.90 (4.66)	-0.49 (2.44)

1. Residual time series were adjusted for precipitation variability (PA).
2. In this instance, numbers between parentheses are the standard deviation of the trend averaged across the different FireMIP models (n=9).

Table S2: Relative trends in burned area for GFED4s and the 9 FireMIP models per region (1997 – 2013, Fig. S18). FireMIP data were available from 1997 – 2013 for all models except the CTEM fire module and JULES-INFERNO (both 1997 – 2012) and MC-Fire (1997 – 2009). Colors indicate increases (red) and decreases (blue) in burned area for each region and time period; significant trends are denoted by asterisks (* p<0.1, ** p<0.05, and *** p<0.01).

Fire product	Trend (% yr^{-1}) with 95% confidence limits														
	World	BONA	TENA	CEAM	NHSA	SHSA	EURO	MIDE	NHAF	SHAF	BOAS	CEAS	SOAS	EQAS	AUST
CLM fire module	-0.17 (0.42)	0.25 (2.10)	1.48 (2.45)	0.20 (2.08)	2.77 (2.66)**	0.14 (1.00)	1.23 (1.16)**	0.28 (0.96)	-1.14 (0.58)***	0.16 (0.82)	0.22 (2.49)	-0.23 (0.69)	0.05 (0.86)	-7.49 (9.44)	1.16 (2.54)
LPJ-GUESS-SIMFIRE-BLAZE	-0.71 (0.57)**	-0.44 (0.97)	1.31 (1.44)*	-0.30 (2.94)	3.00 (3.38)*	-1.64 (1.48)**	-1.31 (2.06)	-0.81 (1.19)	-2.89 (0.73)***	0.55 (0.73)	0.95 (0.75)**	-0.68 (0.99)	-1.24 (1.19)**	-4.76 (8.78)	-0.29 (3.88)
LPJ-GUESS-GlobFIRM	-0.45 (1.61)	-2.57 (3.73)	-0.34 (0.69)	-0.42 (0.40)**	-0.12 (1.90)	-0.38 (0.86)	0.40 (0.70)	-0.15 (2.44)	-1.86 (1.65)**	1.05 (1.06)*	0.07 (0.98)	-0.29 (0.71)	-0.34 (0.47)	-1.87 (1.79)**	-0.32 (12.86)
LPJ-GUESS-SPITFIRE	0.17 (0.63)	1.40 (6.54)	-0.42 (4.97)	-0.07 (2.81)	2.99 (4.23)	0.68 (1.82)	-1.32 (3.94)	1.08 (1.76)	-2.81 (2.05)**	0.95 (0.74)**	-1.98 (6.65)	0.74 (2.48)	-1.86 (2.74)	-2.73 (8.72)	0.92 (3.83)
ORCHIDEE-SPITFIRE	1.02 (0.82)**	0.59 (6.13)	0.76 (5.91)	1.80 (3.56)	2.16 (3.06)	-0.58 (0.89)	-0.23 (1.02)	2.45 (1.41)***	1.14 (0.76)***	0.77 (0.54)***	0.16 (3.29)	-0.82 (1.96)	-1.66 (2.52)	-9.53 (12.33)	2.21 (3.24)
JSBACH-SPITFIRE	0.19 (0.30)	1.84 (2.64)	0.25 (1.47)	1.40 (2.24)	-1.02 (4.21)	-0.19 (0.61)	0.17 (1.19)	0.18 (1.13)	0.07 (0.60)	0.64 (0.62)**	-0.11 (1.60)	-0.02 (0.92)	0.70 (1.87)	-14.17 (17.07)*	0.36 (2.30)
JULES-INFERNO	0.20 (0.57)	0.75 (1.80)	0.10 (2.75)	0.94 (1.02)*	1.70 (1.73)*	-0.20 (1.02)	-0.47 (1.55)	-0.48 (1.99)	0.17 (0.93)	0.05 (0.68)	0.66 (1.65)	0.81 (0.96)*	1.24 (0.79)***	-1.37 (1.74)	-0.39 (2.17)
CTEM fire module	-0.44 (0.77)	0.28 (2.71)	-0.97 (2.66)	-2.26 (1.70)**	2.05 (3.35)	0.71 (1.18)	2.12 (2.00)**	-1.00 (1.43)	-1.99 (0.89)***	-1.15 (1.13)**	-1.55 (3.43)	-0.65 (1.49)	-0.77 (1.62)	-11.33 (14.06)	-0.80 (2.68)
MC-Fire	-1.14 (2.79)	-3.02 (12.99)	-3.74 (12.54)	0.48 (4.35)	0.00 (0.00)	-1.32 (6.59)	4.72 (12.33)	2.22 (7.18)	-0.56 (2.92)	-1.45 (2.52)	-0.44 (12.47)	2.39 (6.42)	-2.45 (5.24)	0.00 (0.00)	-6.82 (9.53)
GFED4s	-1.09 (0.61)***	1.37 (5.60)	2.32 (2.74)*	-2.56 (5.54)	-2.09 (1.79)**	-1.53 (3.55)	-2.75 (4.08)	0.39 (3.41)	-2.03 (0.59)***	0.10 (0.66)	-1.00 (5.38)	-2.24 (2.78)	0.97 (2.01)	-9.26 (9.99)*	-1.69 (4.89)

Table S3: Human influences on modeled burned area. All FireMIP simulations used a standardized set of input variables, with information on historic population and land use taken from Hurtt et al. (*90*) based on the HYDE 3.1 dataset (*89*). For a comprehensive account of the input variables and model details, see Rabin et al. (*34*).

MODEL	Relationship between population and ignitions	Relationship between population and fire size	Influence of cropland on burned area	Influence of livestock and pasture area on burned area	Other human drivers
CLM fire module	Spatially-varying effect on ignitions, and ignition suppression	Suppression of fire size	Cropland fires determined by fuel load, pop. den., GDP, and timing of prescribed fires	No livestock, pasture is treated as grassland	Deforestation fires from LULCC & human fire nr. and size depending on GDP
LPJ-GUESS-SIMFIRE-BLAZE	-	-	No fires on croplands	No livestock, pasture is treated as grassland	Negative relation between population density and burnt area
LPJ-GUESS-GlobFIRM	-	-	No fires on croplands	No livestock, pasture is treated as grassland	-
LPJ-GUESS-SPITFIRE	Regionally modulated effect with highest ignitions for intermediate population density	-	No fires on croplands	No livestock, pasture is treated as grassland	-
ORCHIDEE-SPITFIRE	Regionally modulated effect with highest ignitions for intermediate population density	-	No fires on croplands	N/A (No pastures explicitly simulated)	-
JSBACH-SPITFIRE	Regionally modulated effect with highest ignitions for intermediate population density	Suppression of duration	No fires on croplands	No livestock, pasture is treated as grassland	-
JULES-INFERNO	Spatially-varying effect on ignitions and ignition suppression	-	Croplands are treated as grasslands	No livestock, pasture is treated as grassland	-
CTEM fire module	Spatially-varying effect on ignitions	Suppression of duration	No fires on croplands	N/A (No pastures explicitly simulated)	-
MC-Fire	Anthropogenic suppression	-	No fires on croplands	No livestock, pasture is treated as grassland	-

Table S4: Contributions from changing population and land use to relative trends in burned area in FireMIP models. We disaggregated relative trends in global burned area into component trends from population, land use, and a residual term using FireMIP sensitivity simulations generated by 6 models. Sensitivity simulations held either population or land use constant at 1700 levels. Trends are reported for the 1997 – 2013 period, when both model output and GFED4s data were available. Colors indicate increases (red) and decreases (blue) in burned area and significant trends are denoted by asterisks (* $p<0.1$, ** $p<0.05$, and *** $p<0.01$). Most models produced a net negative effect of increasing population on modeled burned area during 1997 – 2013. The impact of changing land use differed among the models, with three out of six models reporting increased burned area due to land use change. Residual trends represent the combined impact of climate and increasing CO_2, on fire weather, vegetation status, and lightning; five of six models showed an increasing trend in burned area from these factors.

Fire product	Trend (% yr^{-1}) with 95% confidence limits			
	Total	Population	Land use	Residual
LPJ-GUESS-SIMFIRE-BLAZE	-0.71 (0.57)**	-0.57 (0.19)***	-0.42 (0.32)**	0.28 (0.76)
LPJ-GUESS-GlobFIRM	-0.45 (1.61)	-	-0.50 (3.43)	0.05 (4.89)
LPJ-GUESS-SPITFIRE	0.16 (0.63)	0.11 (0.41)	0.22 (0.41)	-0.17 (0.49)
ORCHIDEE-SPITFIRE	1.01 (0.82)**	-0.05 (0.08)	0.24 (0.21)**	0.82 (0.74)**
JSBACH-SPITFIRE	0.19 (0.30)	-0.17 (0.09)***	-0.11 (0.20)	0.47 (0.41)**
JULES-INFERNO	0.20 (0.57)	-0.41 (0.12)***	0.06 (0.10)	0.55 (0.50)**
GFED4s	-1.09 (0.61)***	-	-	-

Table S5: Relative trends in burned area, number of fires, and fire size for MCD64A1 burned area observations and the 3 SPITFIRE-based fire models from 2003 – 2013. Colors indicate increases (red) or decreases (blue) and significant trends are denoted by asterisks (* p<0.1, ** p<0.05, and *** p<0.01). Satellite observations indicated that a decline in the number of fires accounted for most of the declining trend in burned area. In contrast, all three models estimated an increase in the number of fires over this time period, and only LPJ-GUESS-SPITFIRE estimated a decrease in mean fire size. Observed trends in the number of fires and fire size may therefore provide important new data to improve fire models, including the growing influence of human activity on global burned area.

Fire product	Trend (% yr^{-1}) with 95% confidence limits		
	Burned area	Number of fires	Fire size
LPJ-GUESS-SPITFIRE	0.34 (1.61)	0.60 (1.55)	-0.26 (0.44)
ORCHIDEE-SPITFIRE	1.97 (1.42)**	1.07 (0.63)***	0.88 (1.31)
JSBACH-SPITFIRE	0.18 (0.73)	0.07 (0.53)	0.10 (0.71)
MCD64A1	-0.99 (1.67)	-0.81 (1.04)	-0.22 (0.79)

Table S6: Correlation coefficients for the spatial distribution of trends in burned area and trends in satellite-based estimates of atmospheric composition during the peak burning month (absorption aerosol optical depth, aAOD, and surface CO concentrations, Fig. S4b and c) and vegetation indices during the driest month (enhanced vegetation index, EVI, and vegetation optical depth, VOD, Fig. S16). Colors indicate positive correlation (red) and negative correlation (blue); significant correlations are denoted by asterisks (* $p<0.1$, ** $p<0.05$, and *** $p<0.01$). Correlations were based on frequently burning 0.5° grid cells (burned area ≥10% yr^{-1}), and frequently-burning 1° grid cells for CO. Positive correlation between burned area trends and trends in aAOD and CO highlight the global implications of declining burned area for atmospheric chemistry. In South America EVI and VOD exhibited opposite responses to burned area trends (r_{EVI} = -0.22, r_{VOD} = 0.18). Here, decreasing burned area in savannas may have been associated with greater agricultural management and thus greening during the dry season, while aboveground biomass (and water content) declined in response to forest loss from agricultural expansion. Negative correlations in Africa (r_{EVI} = -0.31, r_{VOD} = -0.09) and Australia (r_{EVI} = -0.02, r_{VOD} = -0.28) were consistent with woody encroachment in areas with declining burned area.

	aAOD	CO	EVI	VOD
World	0.26***	0.11***	-0.22***	-0.10***
South America	0.30***	0.50***	-0.22***	0.18***
Africa	0.28***	0.12***	-0.31***	-0.09***
Australia	0.22***	0.17*	-0.02	-0.28***

References and Notes

1. W. J. Bond, F. I. Woodward, G. F. Midgley, The global distribution of ecosystems in a world without fire. *New Phytol.* **165**, 525–538 (2005). doi:10.1111/j.1469-8137.2004.01252.x Medline

2. P. J. Crutzen, M. O. Andreae, Biomass burning in the tropics: Impact on atmospheric chemistry and biogeochemical cycles. *Science* **250**, 1669–1678 (1990). doi:10.1126/science.250.4988.1669 Medline

3. J. Lelieveld, J. S. Evans, M. Fnais, D. Giannadaki, A. Pozzer, The contribution of outdoor air pollution sources to premature mortality on a global scale. *Nature* **525**, 367–371 (2015). doi:10.1038/nature15371 Medline

4. D. M. J. S. Bowman, J. K. Balch, P. Artaxo, W. J. Bond, J. M. Carlson, M. A. Cochrane, C. M. D'Antonio, R. S. Defries, J. C. Doyle, S. P. Harrison, F. H. Johnston, J. E. Keeley, M. A. Krawchuk, C. A. Kull, J. B. Marston, M. A. Moritz, I. C. Prentice, C. I. Roos, A. C. Scott, T. W. Swetnam, G. R. van der Werf, S. J. Pyne, Fire in the Earth system. *Science* **324**, 481–484 (2009). doi:10.1126/science.1163886 Medline

5. R. J. Scholes, S. R. Archer, Tree-grass interactions in savannas. *Annu. Rev. Ecol. Syst.* **28**, 517–544 (1997). doi:10.1146/annurev.ecolsys.28.1.517

6. T. W. Swetnam, J. L. Betancourt, Fire-southern oscillation relations in the southwestern United States. *Science* **249**, 1017–1020 (1990). doi:10.1126/science.249.4972.1017 Medline

7. S. E. Page, F. Siegert, J. O. Rieley, H.-D. V. Boehm, A. Jaya, S. Limin, The amount of carbon released from peat and forest fires in Indonesia during 1997. *Nature* **420**, 61–65 (2002). doi:10.1038/nature01131 Medline

8. M. A. Cochrane, M. D. Schulze, Fire as a recurrent event in tropical forests of the eastern Amazon: Effects on forest structure, biomass, and species composition. *Biotropica* **31**, 2–16 (1999).

9. J. T. Randerson, H. Liu, M. G. Flanner, S. D. Chambers, Y. Jin, P. G. Hess, G. Pfister, M. C. Mack, K. K. Treseder, L. R. Welp, F. S. Chapin, J. W. Harden, M. L. Goulden, E. Lyons, J. C. Neff, E. A. G. Schuur, C. S. Zender, The impact of boreal forest fire on climate warming. *Science* **314**, 1130–1132 (2006). doi:10.1126/science.1132075 Medline

10. D. S. Ward, S. Kloster, N. M. Mahowald, B. M. Rogers, J. T. Randerson, P. G. Hess, The changing radiative forcing of fires: Global model estimates for past, present and future. *Atmos. Chem. Phys.* **12**, 10857–10886 (2012). doi:10.5194/acp-12-10857-2012

11. S. Archibald, A. Nickless, N. Govender, R. J. Scholes, V. Lehsten, Climate and the inter-annual variability of fire in southern Africa: A meta-analysis using long-term field data and satellite-derived burnt area data. *Glob. Ecol. Biogeogr.* **19**, 794–809 (2010). doi:10.1111/j.1466-8238.2010.00568.x

12. O. Pechony, D. T. Shindell, Driving forces of global wildfires over the past millennium and the forthcoming century. *Proc. Natl. Acad. Sci. U.S.A.* **107**, 19167–19170 (2010). doi:10.1073/pnas.1003669107 Medline

13. M. A. Moritz, E. Batllori, R. A. Bradstock, A. M. Gill, J. Handmer, P. F. Hessburg, J. Leonard, S. McCaffrey, D. C. Odion, T. Schoennagel, A. D. Syphard, Learning to coexist with wildfire. *Nature* **515**, 58–66 (2014). doi:10.1038/nature13946 Medline

14. L. E. Aragão, Y. Malhi, N. Barbier, A. Lima, Y. Shimabukuro, L. Anderson, S. Saatchi, Interactions between rainfall, deforestation and fires during recent years in the Brazilian Amazonia. *Philos. Trans. R. Soc. Londn B Biol. Sci.*. **363**, 1779–1785 (2008). doi:10.1098/rstb.2007.0026 Medline

15. N. Andela, G. R. van der Werf, Recent trends in African fires driven by cropland expansion and El Niño to La Niña transition. *Nat. Clim. Chang.* **4**, 791–795 (2014). doi:10.1038/nclimate2313

16. W. M. Jolly, M. A. Cochrane, P. H. Freeborn, Z. A. Holden, T. J. Brown, G. J. Williamson, D. M. J. S. Bowman, Climate-induced variations in global wildfire danger from 1979 to 2013. *Nat. Commun.* **6**, 7537 (2015). doi:10.1038/ncomms8537 Medline

17. I. Bistinas, S. P. Harrison, I. C. Prentice, J. M. C. Pereira, Causal relationships versus emergent patterns in the global controls of fire frequency. *Biogeosciences* **11**, 5087–5101 (2014). doi:10.5194/bg-11-5087-2014

18. S. Archibald, D. P. Roy, B. W. van Wilgen, R. J. Scholes, What limits fire? An examination of drivers of burnt area in Southern Africa. *Glob. Change Biol.* **15**, 613–630 (2009). doi:10.1111/j.1365-2486.2008.01754.x

19. E. Chuvieco, C. O. Justice, in *Advances in Earth Observation of Global Change*, E. Chuvieco, J. Li, X. Yang, Eds. (2010), pp. 187–199.

20. United States Census Bureau, Historical estimates of world population; /www.census.gov.

21. N. Alexandratos, J. Bruinsma, Food and Agriculture Organization, World agriculture towards 2030/2050: The 2012 revision. *ESA Work. Pap. No. 12-03* (2012).

22. N. Ramankutty, A. T. Evan, C. Monfreda, J. A. Foley, Farming the planet: 1. Geographic distribution of global agricultural lands in the year 2000. *Global Biogeochem. Cycles* **22**, GB1003 (2008). doi:10.1029/2007GB002952

23. S. J. Pyne, *Fire in America. A Cultural History of Wildland and Rural Fire* (Princeton Univ.Press, 1982).

24. M. J. E. van Marle *et al*., Historic global biomass burning emissions based on merging satellite observations with proxies and fire models (1750-2015). *Geosci. Model Dev. Discuss.* (2017). doi:10.5194/gmd-2017-32.

25. J. R. Marlon, P. J. Bartlein, C. Carcaillet, D. G. Gavin, S. P. Harrison, P. E. Higuera, F. Joos, M. J. Power, I. C. Prentice, Climate and human influences on global biomass burning over the past two millennia. *Nat. Geosci.* **1**, 697–702 (2008). doi:10.1038/ngeo313

26. J. T. Randerson, Y. Chen, G. R. van der Werf, B. M. Rogers, D. C. Morton, Global burned area and biomass burning emissions from small fires. *J. Geophys. Res.* **117**, G04012 (2012). doi:10.1029/2012JG002128

27. G. R. van der Werf *et al*., Global fire emissions estimates during 1997-2015. *Earth Syst. Sci. Data Discuss.* 10.5194/essd-2016-62 (2017).

28. Materials and methods are available as supplementary materials.

29. L. Giglio, T. Loboda, D. P. Roy, B. Quayle, C. O. Justice, An active-fire based burned area mapping algorithm for the MODIS sensor. *Remote Sens. Environ.* **113**, 408–420 (2009). doi:10.1016/j.rse.2008.10.006

30. D. Mollicone, H. D. Eva, F. Achard, Ecology: Human role in Russian wild fires. *Nature* **440**, 436–437 (2006). doi:10.1038/440436a Medline

31. J. A. Foley, R. Defries, G. P. Asner, C. Barford, G. Bonan, S. R. Carpenter, F. S. Chapin, M. T. Coe, G. C. Daily, H. K. Gibbs, J. H. Helkowski, T. Holloway, E. A. Howard, C. J. Kucharik, C. Monfreda, J. A. Patz, I. C. Prentice, N. Ramankutty, P. K. Snyder, Global consequences of land use. *Science* **309**, 570–574 (2005). doi:10.1126/science.1111772 Medline

32. T. K. Rudel, R. Defries, G. P. Asner, W. F. Laurance, Changing drivers of deforestation and new opportunities for conservation. *Conserv. Biol.* **23**, 1396–1405 (2009). doi:10.1111/j.1523-1739.2009.01332.x Medline

33. H.-W. Lin, J. L. McCarty, D. Wang, B. M. Rogers, D. C. Morton, G. J. Collatz, Y. Jin, J. T. Randerson, Management and climate contributions to satellite-derived active fire trends in the contiguous United States. *J. Geophys. Res. Biogeosci.* **119**, 645–660 (2014). doi:10.1002/2013JG002382 Medline

34. S. S. Rabin, J. R. Melton, G. Lasslop, D. Bachelet, M. Forrest, S. Hantson, J. O. Kaplan, F. Li, S. Mangeon, D. S. Ward, C. Yue, V. K. Arora, T. Hickler, S. Kloster, W. Knorr, L. Nieradzik, A. Spessa, G. A. Folberth, T. Sheehan, A. Voulgarakis, D. I. Kelley, I. C. Prentice, S. Sitch, S. Harrison, A. Arneth, The Fire Modeling Intercomparison Project (FireMIP), phase 1: Experimental and analytical protocols with detailed model descriptions. *Geosci. Model Dev.* **10**, 1175–1197 (2017). doi:10.5194/gmd-10-1175-2017

35. C. Le Quéré, R. Moriarty, R. M. Andrew, G. P. Peters, P. Ciais, P. Friedlingstein, S. D. Jones, S. Sitch, P. Tans, A. Arneth, T. A. Boden, L. Bopp, Y. Bozec, J. G. Canadell, L. P. Chini, F. Chevallier, C. E. Cosca, I. Harris, M. Hoppema, R. A. Houghton, J. I. House, A. K. Jain, T. Johannessen, E. Kato, R. F. Keeling, V. Kitidis, K. Klein Goldewijk, C. Koven, C. S. Landa, P. Landschützer, A. Lenton, I. D. Lima, G. Marland, J. T. Mathis, N. Metzl, Y. Nojiri, A. Olsen, T. Ono, S. Peng, W. Peters, B. Pfeil, B. Poulter, M. R. Raupach, P. Regnier, C. Rödenbeck, S. Saito, J. E. Salisbury, U. Schuster, J. Schwinger, R. Séférian, J. Segschneider, T. Steinhoff, B. D. Stocker, A. J. Sutton, T. Takahashi, B. Tilbrook, G. R. van der Werf, N. Viovy, Y.-P. Wang, R. Wanninkhof, A. Wiltshire, N. Zeng, Global carbon budget 2014. *Earth Syst. Sci. Data* **7**, 47–85 (2015). doi:10.5194/essd-7-47-2015

36. A. Ahlström, M. R. Raupach, G. Schurgers, B. Smith, A. Arneth, M. Jung, M. Reichstein, J. G. Canadell, P. Friedlingstein, A. K. Jain, E. Kato, B. Poulter, S. Sitch, B. D. Stocker, N. Viovy, Y. P. Wang, A. Wiltshire, S. Zaehle, N. Zeng, Carbon cycle. The dominant role of semi-arid ecosystems in the trend and variability of the land CO_2 sink. *Science* **348**, 895–899 (2015). doi:10.1126/science.aaa1668 Medline

37. A. L. Rice, C. L. Butenhoff, D. G. Teama, F. H. Röger, M. A. K. Khalil, R. A. Rasmussen, Atmospheric methane isotopic record favors fossil sources flat in 1980s and 1990s with recent increase. *Proc. Natl. Acad. Sci. U.S.A.* **113**, 10791–10796 (2016). doi:10.1073/pnas.1522923113 Medline

38. W. J. Bond, Ancient grasslands at risk. *Science* **351**, 120–122 (2016). doi:10.1126/science.aad5132 Medline

39. G. P. Hempson, S. Archibald, W. J. Bond, A continent-wide assessment of the form and intensity of large mammal herbivory in Africa. *Science* **350**, 1056–1061 (2015). doi:10.1126/science.aac7978 Medline

40. C. L. Parr, C. E. R. Lehmann, W. J. Bond, W. A. Hoffmann, A. N. Andersen, Tropical grassy biomes: Misunderstood, neglected, and under threat. *Trends Ecol. Evol.* **29**, 205–213 (2014). doi:10.1016/j.tree.2014.02.004 Medline

41. A. F. A. Pellegrini, Nutrient limitation in tropical savannas across multiple scales and mechanisms. *Ecology* **97**, 313–324 (2016). Medline

42. G. R. van der Werf, J. T. Randerson, L. Giglio, G. J. Collatz, M. Mu, P. S. Kasibhatla, D. C. Morton, R. S. DeFries, Y. Jin, T. T. van Leeuwen, Global fire emissions and the contribution of deforestation, savanna, forest, agricultural, and peat fires (1997–2009). *Atmos. Chem. Phys.* **10**, 11707–11735 (2010). doi:10.5194/acp-10-11707-2010

43. L. Giglio, J. T. Randerson, G. R. van der Werf, Analysis of daily, monthly, and annual burned area using the fourth-generation global fire emissions database (GFED4). *J. Geophys. Res. Biogeosci.* **118**, 317–328 (2013). doi:10.1002/jgrg.20042

44. M. Wooster, G. Roberts, G. L. W. Perry, Y. Kaufman, Retrieval of biomass combustion rates and totals from fire radiative power observations: FRP derivation and calibration relationships between biomass consumption. *J. Geophys. Res.* **110** (D24), D24311 (2005). doi:10.1029/2005JD006318

45. K. J. Wessels, S. D. Prince, J. Malherbe, J. Small, P. E. Frost, D. VanZyl, Can human-induced land degradation be distinguished from the effects of rainfall variability? A case study in South Africa. *J. Arid Environ.* **68**, 271–297 (2007). doi:10.1016/j.jaridenv.2006.05.015

46. J. Evans, R. Geerken, Discrimination between climate and human-induced dryland degradation. *J. Arid Environ.* **57**, 535–554 (2004). doi:10.1016/S0140-1963(03)00121-6

47. N. Andela, Y. Y. Liu, A. I. J. M. van Dijk, R. A. M. de Jeu, T. R. McVicar, Global changes in dryland vegetation dynamics (1988–2008) assessed by satellite remote sensing: Comparing a new passive microwave vegetation density record with reflective greenness data. *Biogeosciences* **10**, 6657–6676 (2013). doi:10.5194/bg-10-6657-2013

48. S. M. Herrmann, A. Anyamba, C. J. Tucker, Recent trends in vegetation dynamics in the African Sahel and their relationship to climate. *Glob. Environ. Change* **15**, 394–404 (2005). doi:10.1016/j.gloenvcha.2005.08.004

49. F. Tian, M. Brandt, Y. Y. Liu, K. Rasmussen, R. Fensholt, Mapping gains and losses in woody vegetation across global tropical drylands. *Glob. Chang. Biol.* **23**, 1748–1760 (2017). doi:10.1111/gcb.13464 Medline

50. G. R. van der Werf, J. T. Randerson, L. Giglio, N. Gobron, A. J. Dolman, Climate controls on the variability of fires in the tropics and subtropics. *Global Biogeochem. Cycles* **22**, GB3028 (2008). doi:10.1029/2007GB003122

51. Y. Chen, J. T. Randerson, D. C. Morton, R. S. DeFries, G. J. Collatz, P. S. Kasibhatla, L. Giglio, Y. Jin, M. E. Marlier, Forecasting fire season severity in South America using sea surface temperature anomalies. *Science* **334**, 787–791 (2011). doi:10.1126/science.1209472 Medline

52. G. J. Huffman, D. T. Bolvin, E. J. Nelkin, D. B. Wolff, R. F. Adler, G. Gu, Y. Hong, K. P. Bowman, E. F. Stocker, The TRMM Multisatellite Precipitation Analysis (TMPA): Quasi-Global, Multiyear, Combined-Sensor Precipitation Estimates at Fine Scales. *J. Hydrometeorol.* **8**, 38–55 (2007). doi:10.1175/JHM560.1

53. R. F. Adler, G. J. Huffman, A. Chang, R. Ferraro, P.-P. Xie, J. Janowiak, B. Rudolf, U. Schneider, S. Curtis, D. Bolvin, A. Gruber, J. Susskind, P. Arkin, E. Nelkin, The Version-2 Global Precipitation Climatology Project (GPCP) Monthly Precipitation Analysis (1979–Present). *J. Hydrometeorol.* **4**, 1147–1167 (2003). doi:10.1175/1525-7541(2003)004<1147:TVGPCP>2.0.CO;2

54. G. J. Huffman, R. F. Adler, D. T. Bolvin, G. Gu, Improving the global precipitation record: GPCP Version 2.1. *Geophys. Res. Lett.* **36**, L17808 (2009). doi:10.1029/2009GL040000

55. S. Archibald, D. P. Roy, Identifying individual fires from satellite-derived burned area data. *IEEE Int. Geosci. Remote Sens. Symp. Proc.* **9**, 160–163 (2009).

56. D. Oom, P. C. Silva, I. Bistinas, J. M. C. Pereira, Highlighting biome-specific sensitivity of fire size distributions to time-gap parameter using a new algorithm for fire event individuation. *Remote Sens.* **8**, 663 (2016). doi:10.3390/rs8080663

57. S. Hantson, S. Pueyo, E. Chuvieco, Global fire size distribution is driven by human impact and climate. *Glob. Ecol. Biogeogr.* **24**, 77–86 (2015). doi:10.1111/geb.12246

58. M. C. Hansen *et al*., Towards an operational MODIS continuous field of percent tree cover algorithm: Examples using AVHRR and MODIS data. *Remote Sens. Environ.* **83**, 303–319 (2002). doi:10.1016/S0034-4257(02)00079-2

59. S. Hantson, A. Arneth, S. P. Harrison, D. I. Kelley, I. C. Prentice, S. S. Rabin, S. Archibald, F. Mouillot, S. R. Arnold, P. Artaxo, D. Bachelet, P. Ciais, M. Forrest, P. Friedlingstein, T. Hickler, J. O. Kaplan, S. Kloster, W. Knorr, G. Lasslop, F. Li, S. Mangeon, J. R. Melton, A. Meyn, S. Sitch, A. Spessa, G. R. van der Werf, A. Voulgarakis, C. Yue, The status and challenge of global fire modelling. *Biogeosciences* **13**, 3359–3375 (2016). doi:10.5194/bg-13-3359-2016

60. F. Li, X. D. Zeng, S. Levis, A process-based fire parameterization of intermediate complexity in a dynamic global vegetation model. *Biogeosciences* **9**, 2761–2780 (2012). doi:10.5194/bg-9-2761-2012

61. F. Li, S. Levis, D. S. Ward, Quantifying the role of fire in the Earth system - Part 1: Improved global fire modeling in the Community Earth System Model (CESM1). *Biogeosciences* **10**, 2293–2314 (2013). doi:10.5194/bg-10-2293-2013

62. W. Knorr, L. Jiang, A. Arneth, Climate, CO_2 and human population impacts on global wildfire emissions. *Biogeosciences* **13**, 267–282 (2016). doi:10.5194/bg-13-267-2016

63. B. Smith, D. Wårlind, A. Arneth, T. Hickler, P. Leadley, J. Siltberg, S. Zaehle, Implications of incorporating N cycling and N limitations on primary production in an individual-based dynamic vegetation model. *Biogeosciences* **11**, 2027–2054 (2014). doi:10.5194/bg-11-2027-2014

64. V. Lehsten, K. Tansey, H. Balzter, K. Thonicke, A. Spessa, U. Weber, B. Smith, A. Arneth, Estimating carbon emissions from African wildfires. *Biogeosciences* **6**, 349–360 (2009). doi:10.5194/bg-6-349-2009

65. C. Yue, P. Ciais, P. Cadule, K. Thonicke, S. Archibald, B. Poulter, W. M. Hao, S. Hantson, F. Mouillot, P. Friedlingstein, F. Maignan, N. Viovy, Modelling the role of fires in the terrestrial carbon balance by incorporating SPITFIRE into the global vegetation model ORCHIDEE - Part 1: Simulating historical global burned area and fire regimes. *Geosci. Model Dev.* **7**, 2747–2767 (2014). doi:10.5194/gmd-7-2747-2014

66. C. Yue, P. Ciais, P. Cadule, K. Thonicke, T. T. Van Leeuwen, Modelling the role of fires in the terrestrial carbon balance by incorporating SPITFIRE into the global vegetation model ORCHIDEE -Part 2: Carbon emissions and the role of fires in the global carbon balance. *Geosci. Model Dev.* **8**, 1321–1338 (2015). doi:10.5194/gmd-8-1321-2015

67. G. Lasslop, K. Thonicke, S. Kloster, SPITFIRE within the MPI Earth system model: Model development and evaluation. *J. Adv. Model. Earth Syst.* **6**, 740–755 (2014). doi:10.1002/2013MS000284

68. S. Mangeon, A. Voulgarakis, R. Gilham, A. Harper, S. Sitch, G. Folberth, INFERNO: A fire and emissions scheme for the UK Met Office's Unified Model. *Geosci. Model Dev.* **9**, 2685–2700 (2016). doi:10.5194/gmd-9-2685-2016

69. V. K. Arora, G. J. Boer, Fire as an interactive component of dynamic vegetation models. *J. Geophys. Res.* **110**, G02008 (2005). doi:10.1029/2005JG000042

70. J. R. Melton, V. K. Arora, Competition between plant functional types in the Canadian Terrestrial Ecosystem Model (CTEM) v. 2.0. *Geosci. Model Dev.* **9**, 323–361 (2016). doi:10.5194/gmd-9-323-2016

71. D. Bachelet, K. Ferschweiler, T. J. Sheehan, B. M. Sleeter, Z. Zhu, Projected carbon stocks in the conterminous USA with land use and variable fire regimes. *Glob. Chang. Biol.* **21**, 4548–4560 (2015). doi:10.1111/gcb.13048 Medline

72. B. Bhaduri, E. B. nad Phillip Coleman, J. Dobson, LandScan: Locating people is what matters. *Geoinformatics* **5**, 34–37 (2002).

73. J. E. Dobson, E. A. Bright, P. R. Coleman, R. C. Durfee, B. A. Worley, LandScan: A global population database for estimating populations at risk. *Photogramm. Eng. Remote Sensing* **66**, 849–857 (2000).

74. T. P. Robinson, G. Franceschini, W. Wint, The Food and Agriculture Organization's gridded livestock of the world. *Vet. Ital.* **43**, 745–751 (2007). Medline

75. H. E. Jahnke, Livestock production systems and livestock development in tropical Africa (Kieler Wissenschaftsverlag Vauk, Kiel, Germany, 1982)..

76. M. A. Friedl, D. K. McIver, J. C. F. Hodges, X. Y. Zhang, D. Muchoney, A. H. Strahler, C. E. Woodcock, S. Gopal, A. Schneider, A. Cooper, A. Baccini, F. Gao, C. Schaaf, Global land cover mapping from MODIS: Algorithms and early results. *Remote Sens. Environ.* **83**, 287–302 (2002). doi:10.1016/S0034-4257(02)00078-0

77. Food and Agriculture Organization Statistics devision, FAO (2016); http://faostat3.fao.org.

78. V. R. Pivello, The use of fire in the cerrado and Amazonian rainforests of Brazil: Past and present. *Fire Ecol.* **7**, 24–39 (2011). doi:10.4996/fireecology.0701024

79. G. Hardin, The tragedy of the commons. The population problem has no technical solution; it requires a fundamental extension in morality. *Science* **162**, 1243–1248 (1968). doi:10.1126/science.162.3859.1243 Medline

80. M. Owe, R. A. M. de Jeu, T. Holmes, Multisensor historical climatology of satellite-derived global land surface moisture. *J. Geophys. Res. Earth Surf.* **113**, F01002 (2008).

81. Y. Le Page, D. Oom, J. M. N. Silva, P. Jönsson, J. M. C. Pereira, Seasonality of vegetation fires as modified by human action: Observing the deviation from eco-climatic fire regimes. *Glob. Ecol. Biogeogr.* **19**, 575–588 (2010).

82. H. Lu, M. R. Raupach, T. R. McVicar, D. J. Barrett, Decomposition of vegetation cover into woody and herbaceous components using AVHRR NDVI time series. *Remote Sens. Environ.* **86**, 1–18 (2003). doi:10.1016/S0034-4257(03)00054-3

83. C. S. Potter, J. T. Randerson, C. B. Field, P. A. Matson, P. M. Vitousek, H. A. Mooney, S. A. Klooster, Terrestrial ecosystem production: A process model based on global satellite and surface data. *Global Biogeochem. Cycles* **7**, 811–841 (1993). doi:10.1029/93GB02725

84. R. A. Kahn, B. J. Gaitley, M. J. Garay, D. J. Diner, T. F. Eck, A. Smirnov, B. N. Holben, Multiangle Imaging SpectroRadiometer global aerosol product assessment by comparison with the Aerosol Robotic Network. *J. Geophys. Res. Atmos.* **115**, D23209 (2010). doi:10.1029/2010JD014601

85. M. N. Deeter, S. Martínez-Alonso, D. P. Edwards, L. K. Emmons, J. C. Gille, H. M. Worden, C. Sweeney, J. V. Pittman, B. C. Daube, S. C. Wofsy, The MOPITT Version 6 product: Algorithm enhancements and validation. *Atmos. Meas. Tech.* **7**, 3623–3632 (2014). doi:10.5194/amt-7-3623-2014

86. Y. Chen, D. C. Morton, N. Andela, L. Giglio, J. T. Randerson, How much global burned area can be forecast on seasonal time scales using sea surface temperatures? *Environ. Res. Lett.* **11**, 045001 (2016). doi:10.1088/1748-9326/11/4/045001

87. R. D. Field, G. R. van der Werf, T. Fanin, E. J. Fetzer, R. Fuller, H. Jethva, R. Levy, N. J. Livesey, M. Luo, O. Torres, H. M. Worden, Indonesian fire activity and smoke pollution in 2015 show persistent nonlinear sensitivity to El Niño-induced drought. *Proc. Natl. Acad. Sci. U.S.A.* **113**, 9204–9209 (2016). doi:10.1073/pnas.1524888113 Medline

88. G. R. van der Werf, J. Dempewolf, S. N. Trigg, J. T. Randerson, P. S. Kasibhatla, L. Giglio, D. Murdiyarso, W. Peters, D. C. Morton, G. J. Collatz, A. J. Dolman, R. S. DeFries, Climate regulation of fire emissions and deforestation in equatorial Asia. *Proc. Natl. Acad. Sci. U.S.A.* **105**, 20350–20355 (2008). doi:10.1073/pnas.0803375105 Medline

89. K. Klein Goldewijk, A. Beusen, G. Van Drecht, M. De Vos, The HYDE 3.1 spatially explicit database of human-induced global land-use change over the past 12,000 years. *Glob. Ecol. Biogeogr.* **20**, 73–86 (2011). doi:10.1111/j.1466-8238.2010.00587.x

90. G. C. Hurtt, L. P. Chini, S. Frolking, R. A. Betts, J. Feddema, G. Fischer, J. P. Fisk, K. Hibbard, R. A. Houghton, A. Janetos, C. D. Jones, G. Kindermann, T. Kinoshita, K. Klein Goldewijk, K. Riahi, E. Shevliakova, S. Smith, E. Stehfest, A. Thomson, P. Thornton, D. P. van Vuuren, Y. P. Wang, Harmonization of land-use scenarios for the period 1500-2100: 600 years of global gridded annual land-use transitions, wood harvest, and resulting secondary lands. *Clim. Change* **109**, 117–161 (2011). doi:10.1007/s10584-011-0153-2